

# Inhibition of the *dapE*-Encoded *N*-Succinyl-L,L-diaminopimelic Acid Desuccinylase from *Neisseria meningitidis* by L-Captopril

Anna Starus

*Department of Chemistry and Biochemistry,  
Loyola University-Chicago,  
Chicago, IL*

Boguslaw Nocek

*Center for Structural Genomics of Infectious Diseases,  
Computation Institute, University of Chicago,  
Chicago, IL*

Brian Bennett

*Department of Physics, Marquette University,  
Milwaukee, WI*

James A. Larrabee

*Department of Chemistry and Biochemistry, Middlebury College,  
Middlebury, VT*

Daniel L. Shaw

*Department of Chemistry and Biochemistry, Middlebury College,  
Middlebury, VT*

Wisath Sae-Lee

*Department of Chemistry and Biochemistry, Middlebury College,  
Middlebury, VT*

Marie T. Russo

*Department of Chemistry and Biochemistry, Middlebury College,  
Middlebury, VT*

Danuta M. Gillner

*Department of Chemistry, Silesian University of Technology,  
Gliwice, Poland*

Magdalena Makowska-Grzyska

*Center for Structural Genomics of Infectious Diseases,  
Computation Institute, University of Chicago,  
Chicago, Illinois*

Andrzej Joachimiak\*

*Center for Structural Genomics of Infectious Diseases,  
Computation Institute, University of Chicago,  
Chicago, Illinois*

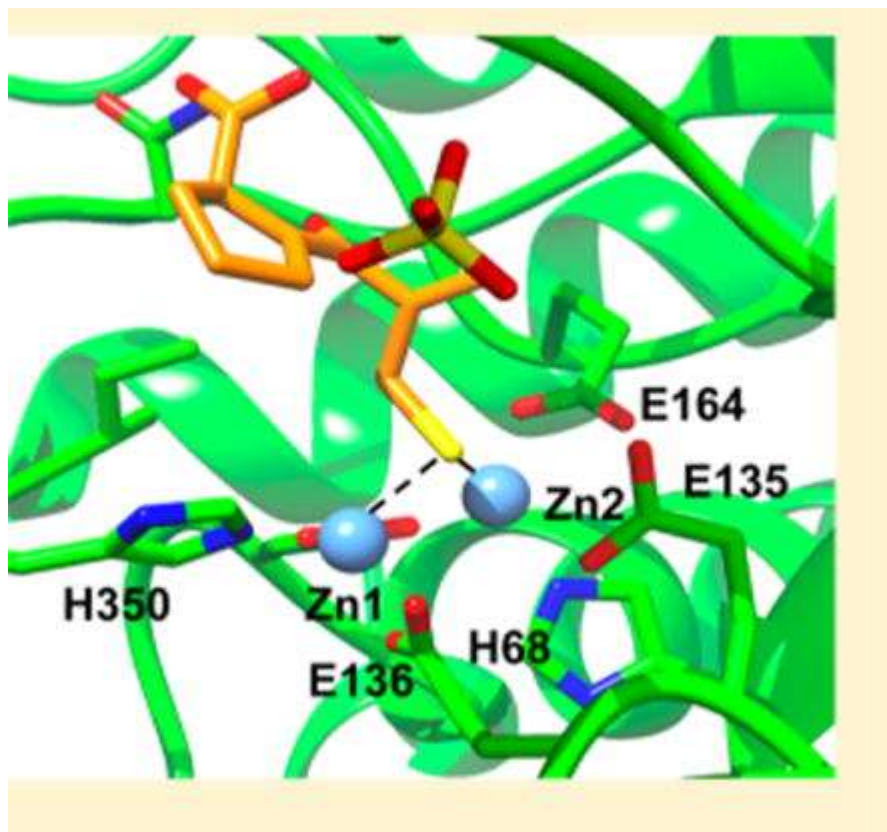
Richard C. Holz\*

*Department of Chemistry, Marquette University,  
Milwaukee, WI*

**Abstract:** Binding of the competitive inhibitor L-captopril to the *dapE*-encoded *N*-succinyl-L,L-diaminopimelic acid desuccinylase from *Neisseria meningitidis* (*NmDapE*) was examined by kinetic, spectroscopic, and crystallographic methods. L-Captopril, an angiotensin-converting enzyme (ACE) inhibitor, was previously shown to be a potent inhibitor of the DapE from *Haemophilus influenzae* (*HiDapE*) with an  $IC_{50}$  of 3.3  $\mu$ M and a measured  $K_i$  of 1.8  $\mu$ M and displayed a dose-responsive antibiotic activity toward *Escherichia coli*. L-Captopril is also a competitive inhibitor of *NmDapE* with a  $K_i$  of 2.8  $\mu$ M. To examine the nature of the interaction of L-captopril with the dinuclear active site of DapE, we have obtained electron paramagnetic resonance (EPR) and magnetic circular dichroism (MCD) data for the enzymatically hyperactive Co(II)-substituted forms of both *HiDapE* and *NmDapE*. EPR and MCD data indicate that the two Co(II) ions in DapE are

antiferromagnetically coupled, yielding an  $S = 0$  ground state, and suggest a thiolate bridge between the two metal ions. Verification of a thiolate-bridged dinuclear complex was obtained by determining the three-dimensional X-ray crystal structure of NmDapE in complex with L-captopril at 1.8 Å resolution. Combination of these data provides new insights into binding of L-captopril to the active site of DapE enzymes as well as important inhibitor-active site residue interaction's. Such information is critical for the design of new, potent inhibitors of DapE enzymes.

### Graphical abstract



Several pathogenic bacteria, some of which were thought to have been eradicated, have made a significant resurgence because of bacterial resistance to antibiotics.<sup>1,2</sup> According to the Centers for Disease Control and Prevention, several bacterial strains currently exhibit multidrug resistance, with >60% of hospital-acquired infections in the United States caused by the so-called ESKAPE pathogens (*Enterococcus faecium*, *Staphylococcus aureus*, *Klebsiella pneumoniae*, *Acinetobacter baumannii*, *Pseudomonas aeruginosa*, and *Enterobacter* species).<sup>3</sup> To alleviate the problem of antibiotic resistance, it is

important that new enzymatic targets be identified and specific inhibitors developed.<sup>4</sup> The *meso*-diaminopimelate (*mDAP*)/lysine biosynthetic pathway offers several potential antibacterial enzyme targets, such as the *dapE*-encoded *N*-succinyl-L,L-diaminopimelic acid desuccinylase (DapE).<sup>5-7</sup> The products of this pathway, *mDAP* and lysine, are essential components of the peptidoglycan cell wall for Gram-negative and most Gram-positive bacteria, providing a link between polysaccharide strands.<sup>6,8,9</sup> DapE genes have been identified in a large number of pathogenic Gram-positive and Gram-negative bacteria, including all of the ESKAPE pathogens.<sup>10-16</sup> Sequence alignment of these DapE genes reveals a minimum of 49% sequence identity. Deletion of the gene encoding DapE is lethal to *Helicobacter pylori* and *Mycobacterium smegmatis* even in the presence of lysine-supplemented media.<sup>10,17</sup> Therefore, DapEs are essential for bacterial cell growth and, as there are no similar biosynthetic pathways in mammals, are targets for inhibitors that may possess antimicrobial activity.<sup>5</sup>

DapEs are metalloenzymes that catalyze the hydrolysis of *N*-succinyl-L,L-diaminopimelic acid (SDAP), forming L,L-diaminopimelic acid and succinate.<sup>8</sup> DapEs have been purified from multiple sources, but the best characterized example is the DapE from *Haemophilus influenzae* (*HiDapE*), which is a homodimeric enzyme (subunit  $M_r$  = 41.6 kDa) that requires two Zn(II) ions per mole of polypeptide for full enzymatic activity.<sup>13</sup> The X-ray crystal structures for both mono- and dinuclear Zn(II) forms of *HiDapE* [ $Zn\_ (HiDapE)$  and  $ZnZn(HiDapE)$ ] have been reported previously.<sup>16</sup> In the dinuclear Zn(II) form, each Zn(II) ion adopts a distorted tetrahedral geometry coordinated by one imidazole (H67 for  $Zn_1$  and H349 for  $Zn_2$ ) and one carboxylate group (E163 for  $Zn_1$  and E135 for  $Zn_2$ ). Both Zn(II) ions are bridged by an additional carboxylate group (D100) and a water/hydroxide, forming a  $(\mu\text{-aquo})(\mu\text{-carboxylato})\text{dizinc(II)}$  core with a 3.3 Å Zn–Zn distance.<sup>16</sup> To date, no X-ray crystallographic data for a DapE–inhibitor complex have been reported.

Thiols are commonly used as inhibitors of Zn(II) metalloproteins because Zn(II) is a relatively soft acid and thiols are soft bases.<sup>18</sup> Examination of several thiol-based compounds led to the identification of moderately strong inhibitors of *HiDapE*.<sup>14,19</sup> For example, L-penicillamine exhibits an  $IC_{50}$  value of 13.7  $\mu\text{M}$  toward *HiDapE* and is a

competitive inhibitor with a measured  $K_i$  of 4.6  $\mu\text{M}$ . DapE is also stereoselective with respect to the recognition of substrate and inhibitors, as D-penicillamine provided an  $\text{IC}_{50}$  value of 50  $\mu\text{M}$ .<sup>14</sup> Similarly, L-captopril, an angiotensin-converting enzyme (ACE) inhibitor, exhibited an  $\text{IC}_{50}$  value of 3.3  $\mu\text{M}$  toward *HiDapE*, while D-captopril yielded an  $\text{IC}_{50}$  value of 42  $\mu\text{M}$ . L-Captopril was shown to be a competitive inhibitor of *HiDapE* with a measured  $K_i$  of 1.8  $\mu\text{M}$  and displayed a dose-responsive antibiotic activity toward *Escherichia coli*.<sup>14</sup> Even though L-captopril is a moderately tight binding inhibitor of DapE enzymes and is a promising lead compound for the development of a novel class of DapE inhibitors, no information about how L-captopril binds to DapE, a requirement for the rational design of new, more potent DapE inhibitors, has been published.

A likely important characteristic of a highly specific, tight binding inhibitor of DapE enzymes will be the molecule's ability to bind to the metal ions in the active site. Several factors are important for interactions of L-captopril with the active site metal ions of DapE, some of which are metal coordination geometry, open metal coordination sites (i.e., those filled by water molecules), and the number of active site metal ions. Therefore, we have analyzed the binding of L-captopril to *HiDapE* and the DapE from *Neisseria meningitidis* (*NmDapE*) via kinetic and spectroscopic methods. We have also determined the X-ray crystal structure of the *NmDapE* enzyme in complex with L-captopril at 1.8 Å resolution. These data provide insight into interactions of L-captopril with the active site metal ions as well as adjacent active site amino acid residues, providing new insight into the rational design of new, more potent inhibitors of DapE enzymes.

## Methods

### Materials

D,L- $\alpha,\epsilon$ -Diaminopimelic acid (98%), succinic anhydride, and ion-exchange resin (Dowex 50WX8-200,  $\text{H}^+$  form) were purchased from Sigma. 2-Naphthalenesulfonic acid 1-hydrate (98%) was purchased from TCI, and microcrystalline cellulose was purchased from Merck. All other chemicals were purchased from commercial sources and were of

the highest quality available. SDAP was synthesized using the procedure described by Lin et al.,<sup>20</sup> providing an overall yield of 41%.

### *Cloning, Expression, and Purification of DapE*

The *HiDapE* enzyme was expressed and purified as described previously.<sup>21</sup> The *DapE* gene from *N. meningitidis* (*NmDapE*) was cloned into the pMCSG7 vector using the ligation-independent cloning method.<sup>22</sup> The following primers were used: 5'-TAC TTC CAA TCC AAT GCC GCA GCT GCA GCT GCA AAA GAA AAA GTG GTT TCG TTG GCA CAA G-3' and 5'-TTA TCC ACT TCC AAT GTT AGT TAG CTA TCC AAT AAA TTC ACT AAC ATT TTG TG-3'. The PCR product was purified using the QIAquick PCR Purification Kit (Qiagen) to remove the primers and dNTPs from the PCR mixture. T4 polymerase was employed to create overhangs on the PCR fragments. The resulting plasmid was transformed into BL21(DE3)/magic *E. coli* competent cells and grown in Luria-Bertani broth containing ampicillin ( $150 \mu\text{g mL}^{-1}$ ) and kanamycin ( $25 \mu\text{g mL}^{-1}$ ) at 37 °C to an  $A_{600}$  of 1.0 while being shaken. IPTG was added (0.4 mM), and culture growth was continued for 16 h at 18 °C. Cells were recovered by centrifugation ( $12000g$ ) for 15 min at 4 °C using a Beckman Coulter Avanti J-E Centrifuge. *NmDapE* was purified according to the standard protocol for Ni-NTA affinity chromatography, and all steps were performed at 4 °C.<sup>23</sup> The His<sub>6</sub> tag was removed by treating each enzyme with His<sub>6</sub>-tagged TEV protease for 16 h at 4 °C in 50 mM HEPES (pH 8.0). Cleaved protein was separated from His<sub>6</sub>-tagged TEV using Ni-NTA affinity chromatography.

### *Enzymatic Assay*

The specific activity of *HiDapE* and *NmDapE* was determined using a 50/50 mixture of D,D- and L,L-SDAP as the substrate in 50 mM phosphate buffer (PP<sub>i</sub>) (pH 7.5) as previously described.<sup>24</sup> The kinetic parameters  $V_{\text{max}}$  and  $K_m$  were determined by quantifying amide bond cleavage (decrease in absorbance) of L,L-SDAP at 225 nm ( $\epsilon = 698 \text{ M}^{-1} \text{ cm}^{-1}$ ) in triplicate using a Shimadzu UV-2450 spectrophotometer equipped with a temperature controller (25 °C). Enzyme activities are expressed as units per milligram, where 1 unit is defined as the amount of enzyme that releases 1  $\mu\text{mol}$  of L,L-SDAP at 30 °C in 1 min. Catalytic activities were determined with an error of



$\pm 10\%$ . Initial rates were fit directly to the Michaelis–Menten equation to obtain the catalytic constants  $K_m$  and  $k_{cat}$  using Origin software.

### *Inhibition of NmDapE by L-Captopril*

The kinetic parameters  $v$  (velocity),  $k_{cat}$  ( $V_{max}/[E]_0$ ),  $K_m$  (Michaelis constant), and  $K_i$  (inhibition constant) were determined in 50 mM phosphate buffer (pH 7.5) spectrophotometrically by recording the initial velocity of the hydrolysis of L,L-SDAP at 25 °C in triplicate.<sup>14</sup> L-Captopril concentrations ranged from 0 to 0.1 mM. The linearity of the progress curves for product formation in the absence and presence of an inhibitor indicated that L-captopril is in rapid equilibrium with NmDapE. The initial rates were plotted against substrate concentration, and the kinetic constants were calculated using Origin software.<sup>20,24,25</sup>

### *Co(II)-Substituted DapE Samples*

Apo-DapE was prepared by extensive dialysis for 72 h at 4 °C against 10 mM EDTA in 50 mM HEPES buffer (pH 7.5). DapE was then exhaustively dialyzed against metal-free (Chelex-100 treated) 50 mM HEPES buffer (pH 7.5). Any remaining metal ions were estimated by comparing the activity of the apoenzyme with that of a sample that had been reconstituted with Zn(II). DapE incubated with EDTA typically had <5% residual activity after dialysis. The mono- and dicobalt(II) forms of *Hi*DapE and *Nm*DapE were prepared using apo-DapE samples that were incubated with  $\text{CoCl}_2$  (99.999%; Strem Chemicals, Newburyport, MA) for 30 min at 25 °C prior to exhaustive dialysis into Chelex-100-treated buffer as previously reported.<sup>26</sup>

### *Electron Paramagnetic Resonance Spectroscopy*

Electron paramagnetic resonance (EPR) spectra were recorded at 4.5–35 K and 9.63 GHz (ER4116DM resonator with  $\mathbf{B}_0 \perp \mathbf{B}_1$ ), 9.37 GHz (ER4116DM resonator with  $\mathbf{B}_0 \parallel \mathbf{B}_1$ ), or 9.39 GHz (SHQ resonator) using 1.2 mT (12 G) magnetic-field modulation at 100 kHz with phase-sensitive detection on a Bruker EleXsys E600 spectrometer equipped with an Oxford Instruments ESR900 helium flow cryostat and ITC503 temperature controller. The SHQ resonator has a  $\mathbf{B}_1$  for a given

microwave power significantly higher than that of the ER4116DM resonator (we estimate by a factor of  $\sim 5$ ). Background signals were collected on samples of frozen buffer and subtracted.

## *Magnetic Circular Dichroism Studies*

The magnetic circular dichroism (MCD) instrument consists of a JASCO J815 spectropolarimeter and an Oxford Instruments SM4000 cryostat/magnet. Variable-temperature variable-field (VTVH) MCD data were collected in increments of 0.5 T (T) from 0 to 7.0 T and at temperatures (nominally) of 1.5, 3.0, 6.0, 12, 24, and 48 K. Spectra were collected at a 1.0 nm bandwidth and scanned at 50 nm/min using a time constant of 1 s. The sample cell has a 0.62 cm path length. Each spectrum was corrected for any natural CD by subtracting the zero-field spectrum of the sample. Even when there is no sample present, the instrument baseline exhibits a small deviation from zero that is both field- and wavelength-dependent. Therefore, each spectrum was also corrected by subtraction of a spectrum recorded at the same magnetic field but with no sample present. The MCD spectra were fit to the minimal number of Gaussian peaks using Grams AI 9.1 after converting the spectra to wavenumber units. In the fitting process, a minimal number of Gaussians were fit to achieve a satisfactory composite spectrum. Fitting of the VTVH MCD data was achieved using a Fortran program, VTVH 2.1.1, written by M. Riley.<sup>27</sup> The spin Hamiltonian and additional details of the fitting program have been described previously.<sup>28</sup> The fits were tested for robustness once a complete set of parameters had been obtained. To do this, the initial parameters were set to the best-fit parameters and then all allowed to float. Subsequently, one key parameter such as  $J$ ,  $D$ ,  $M_{xy}$ ,  $M_{xz}$ , or  $M_{yz}$  was chosen, and its initial value was set differently, after which the fit process was repeated. Percent polarization for a given fit was calculated from  $M_{xy}$ ,  $M_{yz}$ , and  $M_{xz}$  using  $\%M_x = (M_{xy} \times M_{yz})^2 / [(M_{xy} \times M_{xz}) + (M_{xy} \times M_{yz})^2 + (M_{xz} \times M_{yz})^2]$ .  $M_y$  and  $M_z$  were calculated correspondingly.<sup>29</sup> Finally, the VTVH MCD data fitting program used a spin Hamiltonian that included the term  $H = -2JS_1S_2$ .



## *Protein Crystallization*

Prior to crystallization, a 25 mg/mL *NmDapE* protein sample was incubated with 3 equiv of Zn(II) ions and left on ice for 20 min to equilibrate. Zinc(II)-loaded *NmDapE* was screened against 300 commercially available conditions (Index HT and PEG/Ion HT from Hampton Research and Wizard TM from Emerald Biosystems) using a Mosquito liquid handling robot with 96 plates.<sup>30</sup> Several crystallization conditions were characterized yielding diffraction quality crystals. All crystals were screened, and data were collected on the best-diffracting crystals, which were grown by the sitting-drop vapor-diffusion method at 16 °C using 400 nL of a precipitant solution [20% (w/v) PEG 3350 and 100 mM HEPES (pH 7.5)] and 400 nL of [ZnZn(*NmDapE*)]. X-ray quality crystals appeared within 2 weeks. Crystals of [Zn\_*NmDapE*] were also crystallized by the sitting-drop vapor-diffusion method at 16 °C but with a 400 nL precipitant solution [15% (w/v) PEG 3350 and 100 mM succinic acid (pH 7.0)] and 400 nL of a protein, providing crystals within 2 weeks. Crystals of [ZnZn(*NmDapE*)] in complex with L-captopril were obtained by mixing 400 nL of a precipitant solution [0.2 M ammonium acetate, 0.1 M TRIS (pH 8.5), and 25% (w/v) polyethylene glycol 3350] in a 1:1 ratio with a solution of [ZnZn(*NmDapE*)] incubated with a 30 mM solution of L-captopril [50 mM HEPES (pH 7.5) and 150 mM NaCl] with crystals appearing within 3 weeks.

## *Structure Solutions and Refinement*

The X-ray data were collected at beamline 19-ID of the Structural Biology Center at the Advanced Photon Source.<sup>31</sup> All data were processed and scaled using HKL3000.<sup>32</sup> Molecular replacement searches were completed with MOLREP within the CCP4 suite using the structure of apo-*NmDapE* as a template [Protein Data Bank (PDB) entry 1VGY].<sup>16</sup> The asymmetric unit of [Zn\_*(NmDapE)*] (space group  $P2_12_12_1$ ) contains a dimer, while crystals of [ZnZn(*NmDapE*)] and [ZnZn(*NmDapE*)] in complex with L-captopril both crystallized in the  $C222_1$  space group and contained only one subunit of the dimer in the asymmetric unit. Several rounds of rebuilding and readjusting using COOT<sup>33</sup> and refinement using REFMAC<sup>34</sup> and PHENIX<sup>35</sup> improved the initial models. The final models were refined against 95% of the

reflections within the resolution ranges. The remaining 5% of the reflections, which were randomly selected, were used to monitor  $R_{\text{free}}$ . The final refinement statistics are listed in Table 1. Analysis and validation of all structures were performed with the aid of PROCHECK<sup>36</sup> and MOLPROBITY.<sup>37</sup> The refinement restraints for the L-captopril structure were created with the assistance of COOT and were generated from SMILE string.<sup>38</sup>

**Table 1.** Data and Refinement Statistics

	[Zn_NmDapE]	[ZnZn_NmDapE]	[ZnZn_NmDapE]-L-captopril
	Data Collection		
space group	$P2_12_12_1$	$C222_1$	$C222_1$
unit cell ( $\text{\AA}$ )			
	$a = 55.3$	$a = 117$	$a = 116.9$
	$b = 111.4$	$b = 151.6$	$b = 151.5$
	$c = 132.5$	$c = 55.5$	$c = 55.1$
resolution ( $\text{\AA}$ )	39.2–2.09	29.4–2.0	27.5–1.78
wavelength ( $\text{\AA}$ )	0.98	0.98	0.98
no. of observed reflections	204709	202836	178375
no. of unique reflections	48738	33502	46112
redundancy <sup>b</sup>	4.2 (4.0)	6.1 (5.8)	3.9 (3.8)
$R_{\text{merge}}^{\text{a,b}}$ (%)	7.4 (82.1)	8.5 (89.9)	6.5 (75.2)
$R_{\text{pim}}^{\text{a,b}}$ (%)	4.0 (45.7)	4.3 (59.4)	3.3 (44.2)
completeness <sup>b</sup> (%)	99.1 (96.7)	100 (100)	97.7 (99.5)
$I/\sigma$	17.9 (1.5)	22.8 (1.9)	17.7 (1.7)
phasing			
phasing method	MR	MR	MR
	Refinement		
$R_{\text{cryst}}$ (%)	21.3	17.5	16.4
$R_{\text{free}}$ (%)	24.1	20.8	19.6
no. of protein residues	746	374	374
no. of zinc/phosphate/sulfate ions	3/–/4	2/1/–	2/–/1
no. of solvent molecules	380	237	284
rmsd from target values			
bond lengths ( $\text{\AA}$ )	0.003	0.020	0.021
bond angles (deg)	0.71	1.69	1.90
average B factor ( $\text{\AA}^2$ )			
protein	43.8	32.2	24.8
Zn	32.0	23.2	17.9
H <sub>2</sub> O	37.8	24.19	34.6

	[Zn_ <i>NmDapE</i> ]	[ZnZn_ <i>NmDapE</i> ]	[ZnZn_ <i>NmDapE</i> ]-L-captopril
PDB entry	4O23	4PPZ	4PQA
Ramachandran (%) <sup>c</sup>	97.4/2.6	97.6/2/4	97.9/2.1
MF/AA			

<sup>a</sup> $R_{\text{merge}} = \frac{\sum_{hkl} \sum_i |I_i(hkl) - \langle I_{hkl} \rangle|}{\sum_{hkl} \sum_i I_i(hkl)}$ , where  $I_i(hkl)$  is the  $i$ th observation of reflection  $hkl$  and  $\langle I_{hkl} \rangle$  is the weighted average intensity for all observations  $i$  of reflection  $hkl$ .  $R_{\text{pim}} = \frac{\sum_{hkl} [1/(N-1) \sum_i |I_i(hkl) - \langle I_{hkl} \rangle|]}{\sum_{hkl} \sum_i I_i(hkl)}$ .

<sup>b</sup>Numbers in parentheses are values for the highest-resolution bin.

<sup>c</sup>As defined by MOLPROBITY (MF, most favored, AA, additionally allowed).

## PDB Coordinates

The atomic coordinates for [Zn\_*(NmDapE)*], [ZnZn(*NmDapE*)], and [ZnZn(*NmDapE*)] bound by L-captopril were deposited in the PDB as entries 4O23, 4PPZ, and 4PQA, respectively.

## Results

### Kinetic Studies of [Zn\_*(NmDapE)*] and [ZnZn-*(NmDapE)*]

Steady-state kinetic parameters for the hydrolysis of L,L-SDAP by [Zn\_*(NmDapE)*] and [ZnZn(*NmDapE*)] and [Zn\_*(HiDapE)*] and [ZnZn(*HiDapE*)] are listed in Table 2. The kinetic parameters obtained for Zn(II)-loaded *NmDapE* are very similar to those previously reported for Zn(II)-loaded *HiDapE*.<sup>14</sup> Of note is the lack of dependence of  $K_m$  on the zinc content, while the dizinc forms exhibit almost twice the catalytic efficiency of the monozinc forms. L-Captopril was found to be a competitive inhibitor of [ZnZn(*NmDapE*)] with a  $K_i$  of 2.8  $\mu\text{M}$ , a value similar to that observed for [ZnZn(*HiDapE*)] ( $K_i$  of 1.8  $\mu\text{M}$ ).

**Table 2.** Kinetic Constants for [Zn\_*(DapE)*] and [ZnZn(*DapE*)] from *N. meningitidis* and *H. influenza*

	<i>NmDapE</i>		<i>HiDapE</i>	
	Zn	ZnZn	Zn	ZnZn
$K_m$ ( $\mu\text{M}$ )	795 $\pm$ 20	610 $\pm$ 11	730 $\pm$ 15	730 $\pm$ 15
$k_{\text{cat}}$ ( $\text{s}^{-1}$ )	76 $\pm$ 10	120 $\pm$ 10	80 $\pm$ 5	140 $\pm$ 10
$k_{\text{cat}}/K_m$ ( $\text{mM}^{-1} \text{min}^{-1}$ )	5700 $\pm$ 200	11800 $\pm$ 200	6600 $\pm$ 200	11400 $\pm$ 200

## *EPR Spectra of L-Captopril Bound to [Co\_(NmDapE)], [CoCo(NmDapE)], [Co\_(HiDapE)], and [CoCo(HiDapE)]*

EPR spectra of the resting forms of Co(II)-substituted *NmDapE* (Figure 1A) and *HiDapE* (Figure 1B) reveal clear similarities. At 13 K and a nonsaturating microwave power, the [Co\_(DapE)] spectra (traces A in panels A and B of Figure 1) are complex and appear to be due to a moderately rhombic ( $E/D \leq 0.15$ )  $M_S = \pm 1/2$  signal with resonances at  $g' = 5.35$  (1250 G), 4.05 (1660 G), and 2.25 (3015 G), superimposed on an  $M_S = \pm 3/2$  signal with a sharp resonance at  $g' = 6.5$  (1030 G) and a broad derivative feature with an estimated turning point at  $g' \approx 1.15$ . At 4.5 K and a high microwave power (traces B in panels A and B of Figure 1), the  $M_S = \pm 1/2$  signals are almost completely extinguished. This latter behavior indicates that the  $M_S = \pm 1/2$  signals are due to thermal population of the  $M_S = \pm 1/2$  Kramers' doublet at a higher temperature associated with an excited state with a zero-field splitting,  $\Delta$ , on the order of  $10 \text{ cm}^{-1}$  for [Co\_(NmDapE)], and less for [Co\_(HiDapE)], where some  $M_S = \pm 1/2$  contribution is still evident at 4.5 K ( $1 \text{ cm}^{-1}$  corresponds to 1.44 K). If the  $M_S = \pm 1/2$  signals were ground-state signals due to a distinct chemical species, rapid-passage signals would be expected rather than disappearance or diminution of the signals.<sup>39</sup> These data indicate a preferred binding site with an  $M_S = \pm 3/2$  ground state, suggesting a distorted tetrahedral coordination environment.<sup>39</sup>

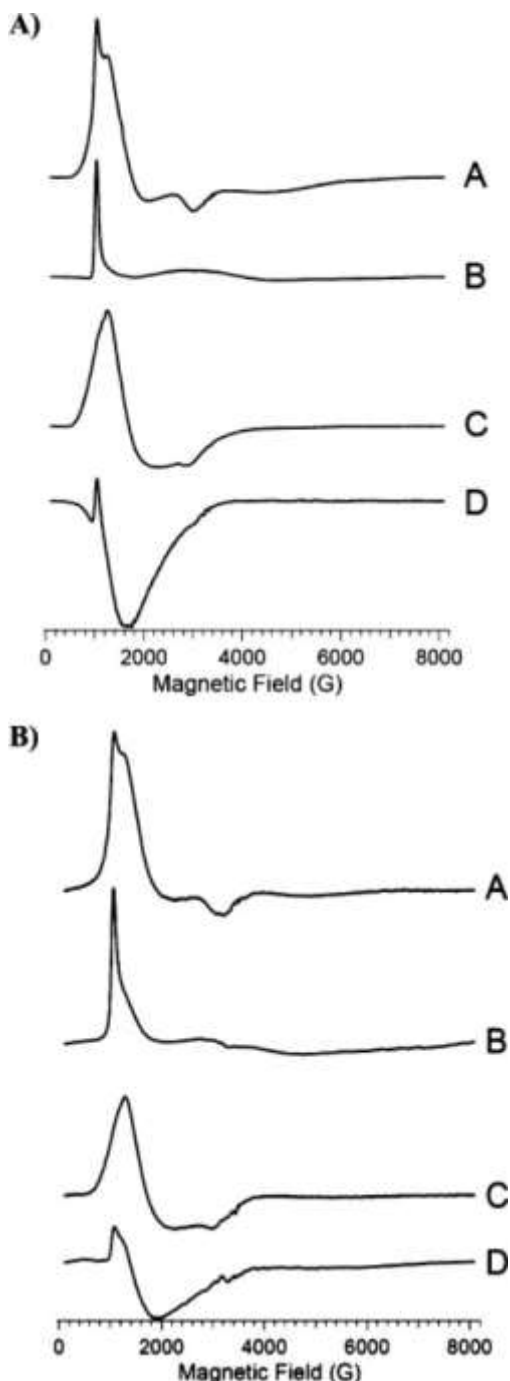


**Figure 1.** (A) EPR spectra at 9.39 GHz (SHQ resonator) of  $[\text{Co}_-(\text{NmDapE})]$  (A and B) and  $[\text{CoCo}(\text{NmDapE})]$  (C and D), recorded at 13 K and 0.5 mW (A and C) and 4.5 K and 100 mW (B and D). Spectral amplitudes are shown normalized for  $1/T$ ,  $(P_{\text{microwave}})^{1/2}$ , and the number of equivalents of Co(II) added. (B) EPR spectra at 9.39 GHz (SHQ resonator) of  $[\text{Co}_-(\text{HiDapE})]$  (A and B) and  $[\text{CoCo}(\text{HiDapE})]$  (C and D), recorded at 13 K and 1.0 mW (A and C) and 4.5 K and 200 mW (B and D). Spectral amplitudes are shown normalized for  $1/T$ ,  $(P_{\text{microwave}})^{1/2}$ , and the number of equivalents of Co(II) added.

Upon addition of a second equivalent of Co(II), a poorly resolved and apparent  $M_S = \pm 1/2$  signal was observed at 13 K (traces C in panels A and B of [Figure 1](#)). In addition, a very weak but clearly identifiable  $^{59}\text{Co}$  hyperfine pattern with  $A_z = 90$  G was observed on the low-field edge of the  $M_S = \pm 1/2$  signal, centered at  $g' = 7.9$  (850 G; see, e.g., [Figure 1A](#), trace C), but is not clearly visible at the scale used in panels A and B of [Figure 1](#). This hyperfine signal could be due to a small amount of an additional  $M_S = \pm 3/2$  signal with  $g_{\text{real}}(z) \sim 2.6$  or else a very rhombic ( $E/D \sim 1/3$ )  $M_S = \pm 1/2$  signal with  $g_{\text{real}}(y) \sim 2.9$ ; the origin of the hyperfine split signal is unclear, but it was completely insensitive to L-captopril and was not considered further.

In contrast to the case for  $[\text{Co}(\text{NmDapE})]$  and  $[\text{Co}(\text{HiDapE})]$ , when EPR spectra of  $[\text{CoCo}(\text{NmDapE})]$  and  $[\text{CoCo}(\text{HiDapE})]$  were recorded at 4.5 K, the predominant  $M_S = \pm 1/2$  signal was clearly still observable as a rapid-passage signal that appeared as an inverted absorption-shaped feature, superimposed on the sharp  $M_S = \pm 3/2$  signal at  $g' = 6.5$  (traces D in panels A and B of [Figure 1](#)). The appearance of a slowly relaxing ground-state  $M_S = \pm 1/2$  signal is consistent with the second added equivalent of Co(II) occupying a five- or six-coordinate site. There is a slight difference between the signals from  $[\text{CoCo}(\text{NmDapE})]$  and  $[\text{CoCo}(\text{HiDapE})]$ . The signal from  $[\text{CoCo}(\text{NmDapE})]$  appears to account for the entire complement of Co(II), whereas that from  $[\text{CoCo}(\text{HiDapE})]$  indicates that some EPR silent Co(II) is present. Further, the  $M_S = \pm 3/2$  signal in  $[\text{CoCo}(\text{HiDapE})]$  is significantly smaller than in  $[\text{Co}(\text{HiDapE})]$  (traces D and B, respectively, in [Figure 1B](#)), whereas this is not the case in  $[\text{CoCo}(\text{NmDapE})]$  (traces D and B, respectively, in [Figure 1A](#); note that in both panels A and B of [Figure 1](#), traces D have been multiplied by 0.5 relative to traces B to account for 2 vs 1 equiv of  $\text{Co}^{2+}$ ). These data suggest a weak antiferromagnetic interaction between the Co(II) ions in  $[\text{CoCo}(\text{HiDapE})]$ , such that  $|J| > h\nu$  for some, but not all, of the population of dinuclear centers in the sample, i.e., that there is a distribution of  $J$  that includes  $0.3 \text{ cm}^{-1}$ . No parallel mode ( $\mathbf{B}_0 \parallel \mathbf{B}_1$ ) EPR signals were observed.



## Addition of L-captopril induced differential effects in [CoCo(NmDapE)] and [CoCo(HiDapE)]

Addition of L-captopril to [CoCo(NmDapE)] resulted in the sharp  $M_S = \pm 3/2$  signal at  $g' = 6.5$  being essentially extinguished, but no overall signal intensity was lost (Figure 2, traces A and B). This is consistent with additional coordination to the hitherto four-coordinate Co(II) ion but no mediation of significant ( $\geq 0.3 \text{ cm}^{-1}$ ) exchange coupling between the two Co(II) ions. In contrast, the addition of L-captopril to [CoCo(HiDapE)] leads to a wholesale loss of  $\sim 30\%$  of the EPR intensity, with no detectable change in line shape (Figure 2, traces C and D), signifying an increase, albeit modest, in the level of exchange coupling between the two Co(II) ions.

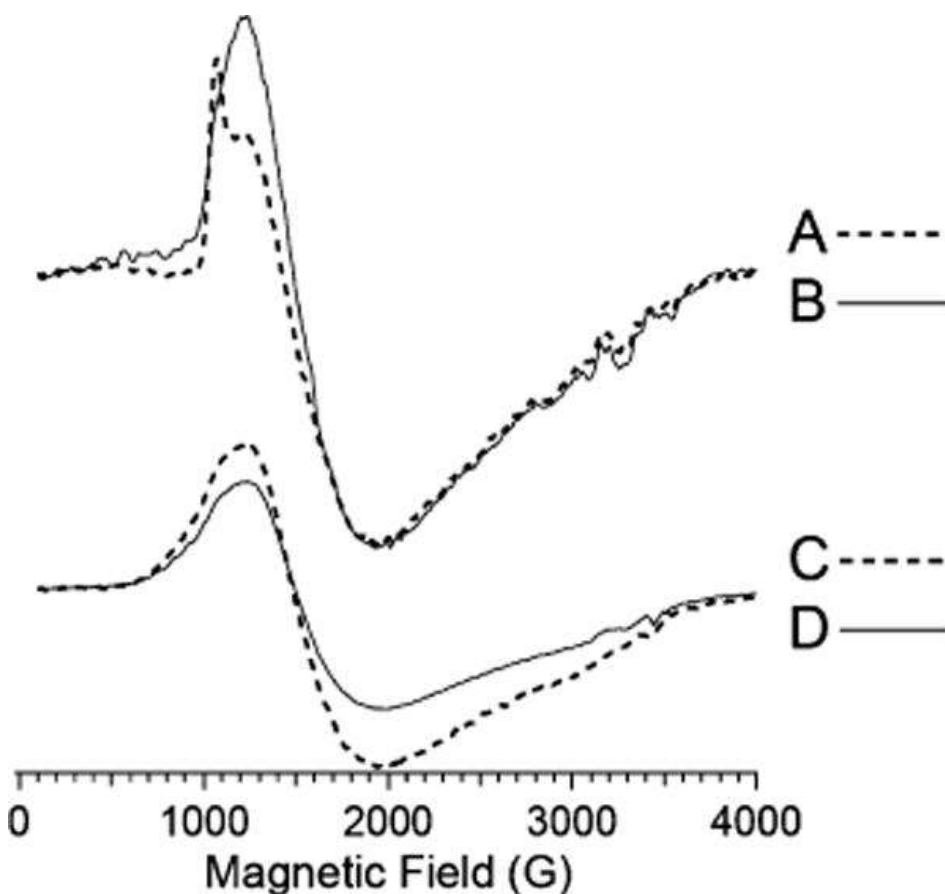


**Figure 2.** EPR spectra at 9.63 GHz (ER4116DM resonator) of [CoCo(NmDapE)] before (A) and after (B) the addition of L-captopril and [CoCo(HiDapE)] before (C) and after (D) the addition of L-captopril. Spectra were recorded at 4.5 K and 100 mW. Spectral amplitudes are shown normalized for  $1/T$ ,  $(P_{\text{microwave}})^{1/2}$ , and the number of equivalents of Co(II) added.

## *MCD Spectra of L-Captopril Bound to [Co\_(NmDapE)], [CoCo(NmDapE)], [Co\_(HiDapE)], and [CoCo(HiDapE)]*

MCD spectra of [CoCo(NmDapE)] and [CoCo(HiDapE)] are nearly identical in shape, band energy, and intensity (Figure 3). It should be noted that the MCD spectra obtained at ambient temperature in the absence of a glycerol glassing agent have the same bands as the low-temperature spectra; however, they are much less intense and broader. All of the bands display temperature-dependent C-terms arising from the paramagnetic high-spin Co(II) ground states. The intense negative band at 576 nm is asymmetric because of a small component at 559 nm in [CoCo(HiDapE)] and at 558 nm in [CoCo(NmDapE)]. This intense negative band along with an intense positive band at 532 nm is characteristic of high-spin Co(II) in a distorted tetrahedral ligand field.<sup>40-42</sup> These bands arise from the  $^4A_2 \rightarrow ^4T_{1(P)}$  d-d transition in  $T_d$  that has been split into three components by the low-symmetry environment in the active site. The negative band at 503 nm along with a very weak positive band at shorter wavelengths is characteristic of high-spin Co(II) in a distorted octahedral ligand field.<sup>40,41,43,44</sup> The band at 503 nm arises from the  $^4T_{1g} \rightarrow ^4T_{1g(P)}$  d-d transition in  $O_h$  that can broaden or split at lower symmetries. The 503 nm band does not split in [CoCo(NmDapE)] or [CoCo(HiDapE)] but is noticeably broader in [CoCo(HiDapE)] than in [CoCo(NmDapE)]. The very weak positive bands at 463 and 475 nm in [CoCo(HiDapE)] and [CoCo(NmDapE)], respectively, are doublet transitions, which gain intensity through spin-orbit coupling to the nearby spin-allowed 503 nm band.<sup>43</sup> Despite the similarity in the MCD spectra of [CoCo(HiDapE)] and [CoCo(NmDapE)], there is a difference in the relative metal binding affinities between the two enzymes. When 1 equiv of Co(II) is added to apo-NmDapE, both the six-coordinate and four-coordinate sites are partially occupied (Figure SI-1 of the Supporting Information). Addition of a second equivalent of Co(II) saturates both binding sites. On the other hand, addition of 1 equiv of Co(II) to apo-HiDapE saturates the four-coordinate site, leaving the six-coordinate site virtually empty (Figure SI-2 of the Supporting Information).

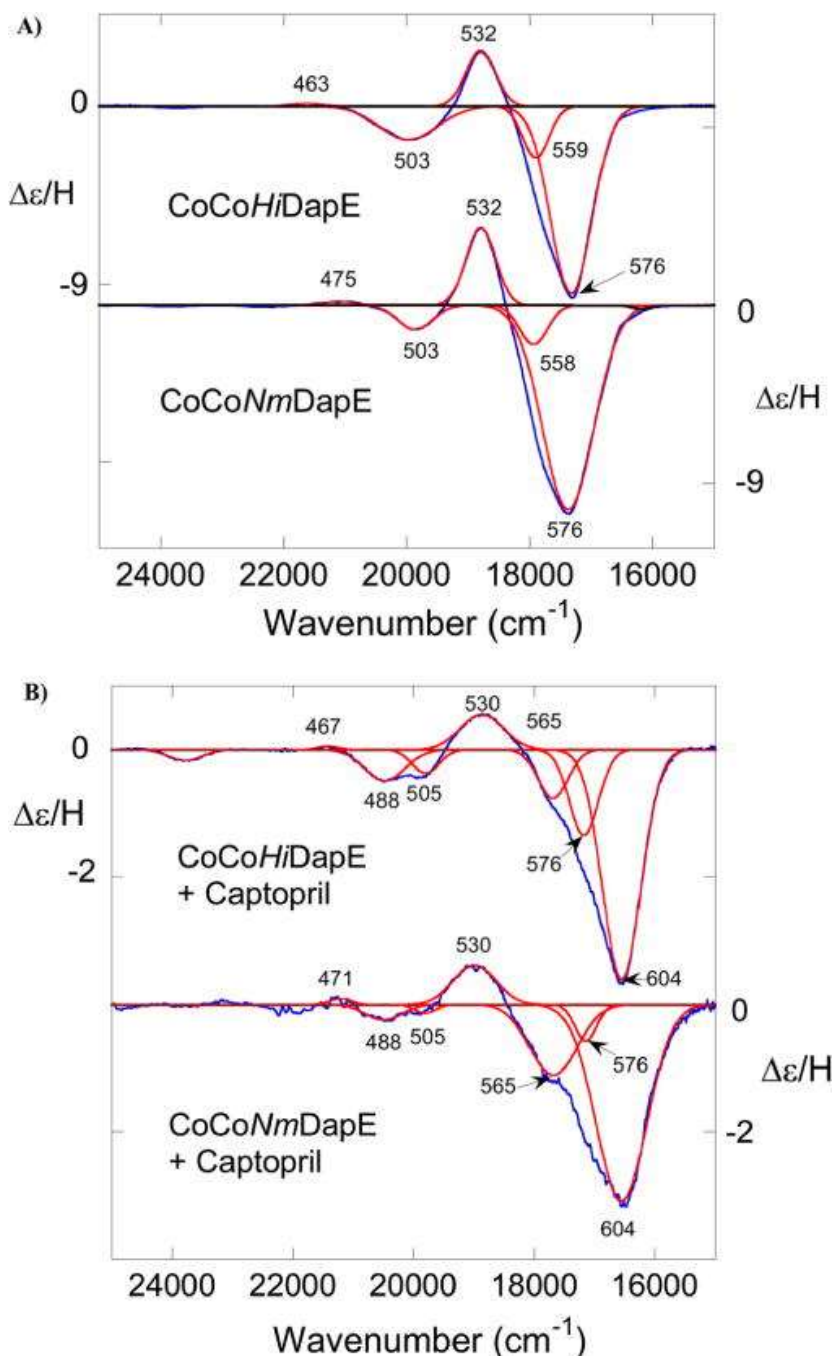


**Figure 3.** MCD spectra of (A) [CoCo(HiDapE)] (top) and [CoCo(NmDapE)] (bottom) and (B) [CoCo(HiDapE)] with 5 equiv of L-captopril (top) and [CoCo(NmDapE)] with 5 equiv of L-captopril (bottom). All spectra were recorded at 1.3 K and 7.0 T in a 0.62 cm path length cell. The enzymes were in a 60/40 (v/v) glycerol/buffer solution. [CoCo(HiDapE)] at 32 mg/mL [0.77 mM enzyme, 1.6 mM in active sites, 3.1 mM in Co(II)]. [CoCo(NmDapE)] at 29 mg/mL [0.70 mM enzyme, 1.4 mM in active sites, 2.8 mM in Co(II)]. The units of  $\Delta\epsilon/H$  are  $\text{M}^{-1} \text{cm}^{-1} \text{T}^{-1}$ , where the concentration of active sites was used. In both panels, the blue trace is the experimental spectrum and the red traces are the Gaussians used to fit the spectra.

VTVH MCD data were collected at 503, 532, and 576 nm on both [CoCo(*NmDapE*)] and [CoCo(*HiDapE*)]. These data were used to construct magnetization plots; typical examples are shown in [Figures SI-3–SI-8 of the Supporting Information](#). The VTVH MCD data were fit as previously described,<sup>27</sup> which yielded the electronic ground-state parameters for magnetic exchange coupling (*J*) and axial (*D*) and rhombic (*E*) zero-field splitting (ZFS). Typical fits are also shown in [Figures SI-3–SI-8 of the Supporting Information](#). Multiple experiments were run, and average values of these parameters along with the standard deviations are given in [Table 3](#). Magnetic exchange coupling, if it occurs, will be strongest through monatomic bridges (e.g.,  $\mu$ -1,1 as opposed to  $\mu$ -1,3). In none of the fittings of the VTVH data from [CoCo(*NmDapE*)] or [CoCo(*HiDapE*)] was the quality of the fit improved (lower value of  $\chi^2$ ) by having a nonzero *J* (positive or negative). This strongly suggests that the bridging oxygen atom is in the form of a  $\mu$ -aqua as opposed to a  $\mu$ -hydroxo. Many dicobalt(II) complexes with either a  $\mu$ -aqua or  $\mu$ -hydroxo have been studied.<sup>8,44–46</sup> Aqua-bridged complexes consistently exhibit a small antiferromagnetic coupling (negative *J*) or no coupling at all, whereas hydroxo-bridged complexes consistently have a small ferromagnetic (positive *J*) coupling. In addition to the previously reported dicobalt(II) complexes, three new model complexes that are consistent with this trend are shown in [Figures SI-13 and SI-14 of the Supporting Information](#). The ZFS parameters that were determined in the fitting of the VTVH data from [CoCo(*NmDapE*)] and [CoCo(*HiDapE*)] were also consistent with assignment of the 503 nm band to a six-coordinate Co(II), and the 532 and 576 nm bands to a distorted four-coordinate Co(II). Generally, the axial ZFS parameter, *D*, is  $>50\text{ cm}^{-1}$  for six-coordinate high-spin Co(II) and  $<10\text{ cm}^{-1}$  for four-coordinate high-spin Co(II).<sup>8,42</sup>

**Table 3.** VTVH MCD Fitting Parameters

parameter	[CoCo( <i>NmDapE</i> )] <sup>a</sup>	[CoCo( <i>NmDapE</i> )] and captopril <sup>b</sup>	[CoCo( <i>HiDapE</i> )] <sup>c</sup>	[CoCo( <i>HiDapE</i> )] and captopril <sup>d</sup>
<i>J</i> (cm <sup>-1</sup> )	0	-0.1	0	-0.05 ± 0.04
<i>D</i> (cm <sup>-1</sup> ), 4C	3.7 ± 0.6	0.05	3.7 ± 1.0	4.1 ± 1.5
<i>E/D</i> , 4C	~0	0.002	~0	0.25 ± 0.14
<i>D</i> (cm <sup>-1</sup> ), 6C	>100	>50	>100	28 ± 5
<i>E/D</i> , 6C	0.18 ± 0.04	~0	0.27 ± 0.04	0.08 ± 0.03
polarization	503 nm x-pol. 532 nm xy-pol.	505 nm na 530 nm na	503 nm x-pol. 532 nm xy-pol.	505 nm z-pol. 530 nm z-pol.

parameter	[CoCo( <i>NmDapE</i> )] <sup>a</sup>	[CoCo( <i>NmDapE</i> )] and captopril <sup>b</sup>	[CoCo( <i>HiDapE</i> )] <sup>c</sup>	[CoCo( <i>HiDapE</i> )] and captopril <sup>d</sup>
	576 nm xy-pol.	604 nm z-pol.	576 nm xy-pol.	604 nm z-pol.

<sup>a</sup>Based on three independent experiments;  $\pm$ one standard deviation.

<sup>b</sup>Based on a single experiment.

<sup>c</sup>Based on eight independent experiments.

<sup>d</sup>Based on four independent experiments.

The addition of 1 equiv (based on the concentration of active sites) of L-captopril to either [CoCo(*HiDapE*)] or [CoCo-(*NmDapE*)] has no apparent effect on the MCD spectra. However, addition of 5 equiv of L-captopril causes the green resting enzyme solutions to turn blue (Figure 3B). The four-coordinate Co(II) bands shift from 532, 559, and 576 nm in [CoCo(*HiDapE*)] to 530, 565, and 604 nm, respectively, in the [CoCo(*HiDapE*)]-L-captopril complex, while the bands for the same species shift from 532, 558, and 576 nm in [CoCo(*NmDapE*)] to 530, 565, and 604 nm, respectively, in the [CoCo(*NmDapE*)]-L-captopril complex. The six-coordinate band at 503 nm splits into two bands at 488 and 505 nm for the [CoCo(*HiDapE*)]-L-captopril and [CoCo(*NmDapE*)]-L-captopril complexes. There is a small peak at 576 nm in both spectra, which is due to uncomplexed enzyme. In addition to these band shifts, there is a roughly 3-fold decrease in MCD intensity, which is not due to loss of Co(II) from the enzyme caused by L-captopril. Finally, the quality of the optical glasses formed in the presence of L-captopril is not as high as for the resting enzyme alone. The resulting MCD spectra had signal-to-noise ratios considerably lower than those of the MCD spectra obtained for the resting enzymes.

VT VH MCD data were also collected on the 505, 530, and 604 nm bands in the [CoCo(*HiDapE*)]-L-captopril complex and only for the 604 nm band in the [CoCo(*NmDapE*)]-L-captopril complex. Example magnetization plots and fits are shown in Figures SI-9-SI-12 of the Supporting Information. The  $\chi^2$  values for fits of the 505 and 530 nm data are quite high as is the  $\chi^2$  value for the 604 nm data for the [CoCo-(*NmDapE*)]-L-captopril complex. The best fits were obtained with a small negative value for  $J$ . In addition, the ZFS parameters for both the six- and four-coordinate sites changed but were still in the ranges expected for the corresponding Co(II) species (Table 3).

## Crystal Structures of [Zn<sub>1</sub>(NmDapE)], [ZnZn(NmDapE)], and the L-Captopril-Bound [ZnZn(NmDapE)] Complex

The X-ray crystal structures of [Zn<sub>1</sub>(NmDapE)] (2.1 Å), [ZnZn(NmDapE)] (2.0 Å), and the [ZnZn(NmDapE)]-L-captopril complex (1.8 Å) were determined. These three structures along with that of apo-NmDapE, which was previously determined (PDB entry 1VGY),<sup>47</sup> reveal the typical two-domain homodimer structure (either present in the asymmetric unit or generated by the crystallographic 2-fold axis) observed for all DapE enzymes. Comparison of all four structures of NmDapE shows that the overall fold is well-preserved and the structures of the apo, monozinc, dizinc, and L-captopril-bound forms are nearly identical. Each of these structures overlays with an rmsd for Ca atoms of 0.59 Å {apo-NmDapE over [Zn<sub>1</sub>(NmDapE)]} and 0.73 Å {apo-NmDapE over [ZnZn(NmDapE)] and L-captopril-bound [ZnZn(NmDapE)]}. Close analysis of the [ZnZn(NmDapE)] and [ZnZn(NmDapE)]-L-captopril structures [both were determined from isomorphous crystals grown under similar conditions (Table 1)] reveals that inhibitor binding does not introduce any significant changes into the structure as evidenced by a very low rmsd of 0.2 Å. Furthermore, examination of the active site regions of the [ZnZn(NmDapE)] structure indicates that the metal ions and ligands are in nearly identical positions. The dinuclear Zn(II) active sites in both [ZnZn(NmDapE)] and the [ZnZn(NmDapE)]-L-captopril complex adopt coordination geometries identical to that reported for HiDapE.<sup>16</sup>

For [ZnZn(NmDapE)], the first metal binding site, Zn<sub>1</sub>, resides in a distorted tetrahedral geometry and is bound by the carboxylate OD1 atom of D101 and OE1 atom of E164 as well as the NE1 atom of H68. The Zn<sub>2</sub> metal ion resides in a distorted trigonal bipyramidal geometry and is bound by the NE2 atom of H350, two oxygen atoms, OD2 from D101 and OE2 from E136, and the O1 atom of ethylene glycol. Interestingly, for [Zn<sub>1</sub>(NmDapE)] a full dimer resides in the asymmetric unit, and Zn(II) binding is different between the two active sites. In one of the active sites, a single Zn(II) ion is bound in the first metal binding site, while in the second active site, two Zn(II) ions are present but with occupancies modeled at 60% for Zn<sub>1</sub> and 18% for Zn<sub>2</sub>. These data suggest that metal binding is not strictly



sequential for *NmDapE*, which is different from that observed for *HiDapE*.

The 1.8 Å structure of the [ZnZn(*NmDapE*)]–L-captopril complex reveals clear electron density corresponding to L-captopril inside the positively charged groove, formed between the catalytic and dimerization domains (Figure 4). The sulfhydryl group of L-captopril bridges the two active site Zn(II) ions with Zn–S distances of 2.3 Å, displacing the bridging water molecule. The carboxylate of the proline moiety of L-captopril forms a hydrogen bond with N346 (ND2–O3, 3.0 Å) and the amide of G325 (N–O2, 2.9 Å). It also makes a strong hydrogen bond with the hydroxyl of Y198 (OH–O3, 2.5 Å), which reaches over from the second subunit of the dimer. The O1 peptide carbonyl oxygen of L-captopril forms a hydrogen bond with a well-ordered water molecule (2.8 Å) that is stabilized by its interaction with R179 (NH2–O, 3.1 Å) and P165 (2.6 Å).

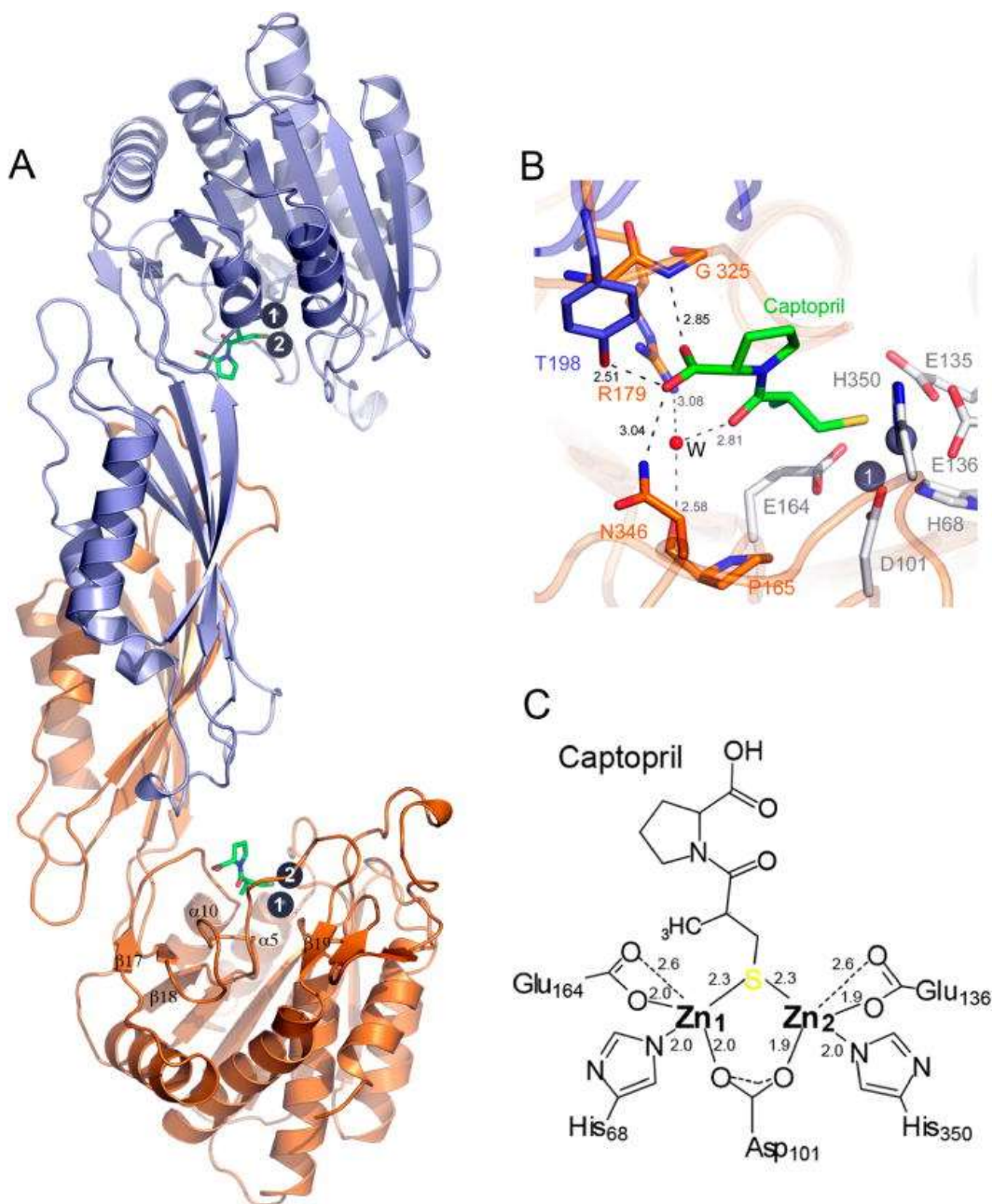


**Figure 4.** Structure of the [ZnZn(NmDapE)]-L-captopril complex. (A) Ribbon diagram of the homodimer of [ZnZn(NmDapE)] (subunit A colored orange and subunit B blue). The Zn(II) ions in the dinuclear active site are shown as black spheres, while molecules of L-captopril are shown as green sticks. (B) Close-up of the active site region showing the hydrogen bonding interactions of L-captopril (green) with surrounding protein residues and solvent molecule (red sphere). The active site residues are color-coded (orange and blue sticks) according to the subunit coloring, while the conserved residues binding to the Zn(II) ions are colored gray. (C) Schematic drawing of the dinuclear Zn(II) active site bound by L-captopril (distances in angstroms).

## Discussion

EPR spectra of  $[\text{Co}(\text{NmDapE})]$  and  $[\text{Co}(\text{HiDapE})]$  suggest the first Co(II) ion to bind resides in a distorted tetrahedral coordination geometry at low temperatures, and this assignment is consistent with the crystallographic and MCD data. EPR spectra of  $[\text{CoCo}(\text{NmDapE})]$  and  $[\text{CoCo}(\text{HiDapE})]$  suggest a five- or six-coordinate Co(II) ion in the second metal binding site. The EPR data also indicate an antiferromagnetic interaction due to the formation of a spin-coupled species with  $|J| > 0.3 \text{ cm}^{-1}$  between the Co(II) ions in  $[\text{CoCo}(\text{HiDapE})]$  but no interaction was detected in  $[\text{CoCo}(\text{NmDapE})]$ ;<sup>24</sup> some 30% of the Co(II) in  $[\text{CoCo}(\text{HiDapE})]$  is EPR silent. EPR of the L-captopril complexes of both  $[\text{CoCo}(\text{NmDapE})]$  and  $[\text{CoCo}(\text{HiDapE})]$  indicated that the hitherto tetrahedral Co(II) ion acquired an additional ligand(s) and modulated the spin coupling in the latter (Figure 2), consistent with the captopril-derived thiolate bridge observed in the crystal structure (Figure 4). For both  $[\text{CoCo}(\text{NmDapE})]$  and  $[\text{CoCo}(\text{HiDapE})]$ , characteristic MCD bands for high-spin Co(II) in a distorted tetrahedral and distorted octahedral ligand field are observed (Figure 3), consistent with EPR data. An interesting finding is that despite the similarity in the MCD spectra between  $[\text{CoCo}(\text{NmDapE})]$  and  $[\text{CoCo}(\text{HiDapE})]$ , the spectra obtained for  $[\text{CoCo}(\text{NmDapE})]$  reveal that both the four- and six-coordinate sites are occupied upon the addition of only 1 equiv of Co(II), suggesting a less than strictly sequential binding model for *NmDapE* that is not observed for *HiDapE*. This finding is consistent with EPR data as well as the X-ray crystal structure of  $[\text{Zn}(\text{NmDapE})]$ .

Correlation of the ZFS observed by MCD with coordination number was used as a coordination number indicator (termed the CN/ZFS correlation). In the CN/ZFS correlation, four-coordinate Co(II) exhibits  $\text{ZFS} < 13 \text{ cm}^{-1}$ , also observed directly here by EPR; five-coordinate between 20 and  $50 \text{ cm}^{-1}$ ; and six-coordinate above  $50 \text{ cm}^{-1}$ .<sup>48</sup> The ZFS parameters determined from fits of VTVH data for  $[\text{CoCoNmDapE}]$  and  $[\text{CoCoHiDapE}]$  are consistent with four-coordinate and six-coordinate Co(II) centers in the active site. On the basis of previously published magnetic properties of several  $\mu$ -aqua  $\mu$ -hydroxo dicobalt(II) model complexes, weak to moderately strong antiferromagnetic coupling would be expected from a single oxygen

atom bridge.<sup>49,50</sup> Fitting of the VTVH data from [CoCoNmDapE] and [CoCoHiDapE] strongly suggests that the bridging oxygen atom, in the resting enzyme, is due to  $\mu$ -aqua as opposed to  $\mu$ -hydroxo moieties. MCD data of the L-captopril complexes are consistent with the thiol of L-captopril bridging the two active site Co(II) ions, producing an antiferromagnetically coupled dicobalt(II) center with an  $S = 0$  ground state. The overall changes strongly suggest that L-captopril displaces the bridging water molecule and binds to both metal ions through a monatomic bridge whose ligand-field strength is less than that of water. These findings are consistent with EPR data for [CoCoHiDapE] bound by L-captopril. Taken together, the optical, magneto-optical, and EPR results are in strong agreement and indicate that L-captopril interacts directly with both metal ions.

Additional structural information was obtained from X-ray crystallography, including the finding that no active site ligands are displaced upon L-captopril binding except for replacement of the water molecule that bridges the two Zn(II) ions in the wild-type enzyme by the L-captopril-derived thiolate sulfur atom. The remainder of the molecular structure of DapE is barely perturbed, but some significant hydrogen bonds to L-captopril that likely identify residues important for substrate and inhibitor recognition and/or binding are formed. The binding of L-captopril to the dinuclear active site of [ZnZn-(NmDapE)] provides the first structural data for an inhibited form of any DapE enzyme, providing a model for inhibitor design as well as enzyme-substrate interactions.

Inspection of the X-ray crystal structures of [Zn<sub>2</sub>(NmDapE)] and [ZnZn(NmDapE)], combined with surface analysis, reveals a deep groove that extends along the borders of the catalytic and dimerization domains and houses the active site. This well-defined and negatively charged cavity is shaped from the top by strand  $\beta$ 17 and  $\alpha$ 10 and in the middle by the loop connecting these two elements (residues 321–328). The bottom of the cavity is formed by a loop (residues 132–142) connecting  $\beta$ -strands  $\beta$ 6 and  $\alpha$ 5 and a loop (residues 341–355) connecting  $\beta$ 18 and  $\beta$ 19. Because the substrate has a linear shape, we predict that it binds in an extended conformation, lining up along the groove with the peptide bond positioned right over the active site metals. DapE enzymes have strict specificity for the L,L-isoform of SDAP.<sup>24</sup> This specificity is built into the active site that includes both

the dinuclear metal cluster and adjacent amino acid residues that form a substrate binding cavity groove. Several studies indicate that substrate binding pockets play an important role in substrate recognition and binding for metallohydrolases.<sup>51-53</sup> Insight into the role of this cavity comes from the structure of the [ZnZn(*NmDapE*)]-L-captopril complex as several interactions between the inhibitor and residues within this cavity are formed. The L-captopril peptide bond forms a hydrogen bond with a well-ordered water molecule, which is stabilized by R179 and P165. In addition, the carboxyl terminus of the dipeptide is held in position by ionic interactions between N346 and G325. Interestingly, the carboxyl group also forms a hydrogen bond with the hydroxyl moiety of Y198, which resides on the other subunit of the dimer. This interaction is of great interest, because it is the first evidence of a residue from the second subunit interacting with an inhibitor bound to the first subunit. These data suggest a heretofore unknown function for dimer formation of DapE enzymes. Specifically, this indicates that the dimerization domain not only is crucial for dimer formation but also could play an important role in substrate recognition and binding. This is consistent with the findings that dimerization domain deletion mutants of *HiDapE* are inactive, highlighting the importance of DapE dimer formation.<sup>16</sup>

In summary, a major limitation in developing a previously undescribed class of antimicrobials that target DapE enzymes has been the lack of knowledge about binding of the inhibitor to the DapE active site, including potential residues involved in substrate recognition and binding. We have spectroscopically and crystallographically characterized the binding of the competitive inhibitor L-captopril to DapE. The thiol moiety of L-captopril coordinates to both active site metal ions in a  $\mu$ -thiolate fashion. No other inhibitor-centered ligands interact with the active site metal ions. Analysis of the first X-ray crystal structure of a DapE enzyme bound to an exogenous ligand, the [ZnZn(*NmDapE*)]-L-captopril complex, allowed for identification of several important active site pocket residues. These include R179, P165, and N346 that form hydrogen bonds to the functional groups of L-captopril. Remarkably, Y198 from one subunit was discovered to be involved in hydrogen bond formation with the L-captopril bound to the active site of the opposite subunit. This unforeseen hydrogen bonding interaction may be critical for catalysis and may also prove to be crucial in the development of novel medicinal chemistry leads. Because

L-captopril is an angiotensin-converting enzyme (ACE) inhibitor and a moderately strong inhibitor of DapE enzymes, understanding the electronic and structural properties of binding of L-captopril to the active site of DapE provides a foundation for the design of new, more potent DapE inhibitors.

## Acknowledgments

Results mentioned in this report are derived from work performed at Argonne National Laboratory, Structural Biology Center at the Advanced Photon Source, and at the National Biomedical EPR Center at the Medical College of Wisconsin (MCW). Argonne is operated by University of Chicago Argonne, LLC, for the U.S. Department of Energy, Office of Biological and Environmental Research, under Contract DE-AC02-06CH11357. The MCW EPR Center is funded by National Institutes of Health Grant P41 EB001980 to James S. Hyde.

**Funding** This research has been funded in part by National Institutes of Health Grants R15 AI085559-01A1 (R.C.H.) and GM094585 (A.J.), Contract HHSN272201200026C (A.J.), and Grant P41 EB001980 (B.B.), the U.S. Department of Energy, Office of Biological and Environmental Research, under Contract DE-AC02-06CH11357, National Science Foundation (J.A.L., D.L.S., and W.S.-L.) Grants CHE-0848433, CHE-1303852, and CHE-0820965 (MCD instrument), and the Arnold and Mabel Beckman Foundation (D.L.S.).

## Abbreviations

L,L-SDAP	<i>N</i> -succinyl-L,L-diaminopimelic acid
DapE	<i>dapE</i> -encoded <i>N</i> -succinyl-L,L-diaminopimelic acid desuccinylase
<i>m</i> DAP	<i>meso</i> -diaminopimelic acid
Hepes	4-(2-hydroxyethyl)-1-piperazineethanesulfonic acid
PCR	polymerase chain reaction
IPTG	isopropyl $\beta$ -D-1-thiogalactopyranoside
NTA	nitrilotriacetic acid
IMAC	immobilized metal affinity chromatography
SDS-PAGE	sodium dodecyl sulfate-polyacrylamide gel electrophoresis
SSM	secondary structure matching algorithm
rmsd	root-mean-square deviation
MCD	magnetic circular dichroism
VT VH	variable-temperature variable-field
EPR	electron paramagnetic resonance
EXAFS	extended X-ray absorption fine structure



## Footnotes

## Supporting Information

MCD spectra of *NmDapE* (Figure SI-1) and *HiDapE* (Figure SI-2), magnetization plots of the VTVH MCD data (Figures SI-3–SI-12), the structure of  $[\text{Co}_2(\mu\text{-OH})(\mu\text{-1,3-CF}_3\text{COO})_2(\text{Me}_3\text{TACN})_2]^+$  and the associated MCD spectrum (Figure SI-13), and the structure of CoF and CoH and the associated MCD spectra (Figure SI-14). The Supporting Information is available free of charge on the ACS Publications website at DOI: 10.1021/acs.biochem.5b00475.

The authors declare no competing financial interest.

## References

- <sup>1</sup>Levy SB. The Challenge of Antibiotic Resistance. *Sci Am.* 1998;278:46–53.
- <sup>2</sup>Nemecek S. Beating Bacteria. New ways to Fend off Antibiotic-Resistant Pathogens. *Sci Am.* 1997;276:38–39.
- <sup>3</sup>Rice LB. Federal Funding for the Study of Antimicrobial Resistance in Nosocomial Pathogens: No ESKAPE. *J Infect Dis.* 2008;197:1079–1081.
- <sup>4</sup>Supuran CT, Scozzafava A, Clare BW. Bacterial Protease Inhibitors. *Med Res Rev.* 2002;22:329–372.
- <sup>5</sup>Scapin G, Blanchard JS. Enzymology of Bacterial Lysine Biosynthesis. *Adv Enzymol.* 1998;72:279–324.
- <sup>6</sup>Coates ARM, Hu Y. Novel approaches to developing new antibiotics for bacterial infections. *Br J Pharmacol.* 2007;152:1147–1154.
- <sup>7</sup>Goldman M. Reflections on the Innovative Medicines Initiative. *Nat Rev Drug Discovery.* 2011;10:321–322.
- <sup>8</sup>Born TL, Zheng R, Blanchard JS. Hydrolysis of *N*-succinyl-L,L-Diaminopimelic Acid by the *Haemophilus influenzae* *dapE*-Encoded Desuccinylase: Metal Activation, Solvent Isotope Effects, and Kinetic Mechanism. *Biochemistry.* 1998;37:10478–10487.
- <sup>9</sup>Howe RA, Bowker KE, Walsh TR, Feest TG, MacGowan AP. Vancomycin-resistant *Staphylococcus aureus*. *Lancet.* 1998;351:602.
- <sup>10</sup>Pavelka MS, Jr, Jacobs WR., Jr Biosynthesis of Diaminopimelate, the Precursor of Lysine and a Component of Peptidoglycan, is an Essential Function of *Mycobacterium smegmatis*. *J Bacteriol.* 1996;178:6496–6507.
- <sup>11</sup>Rowell S, Pauptit RA, Tucker AD, Melton RG, Blow DM, Brick P. Crystal Structure of Carboxypeptidase G2, a Bacterial Enzyme with Applications in Cancer Therapy. *Structure.* 1997;5:337–347.

- <sup>12</sup>Desmarais W, Bienvenue DL, Bzymek KP, Petsko GA, Ringe D, Holz RC. The High-Resolution Structures of the Neutral and the Low pH Crystals of the Aminopeptidase from *Aeromonas proteolytica*. *JBIC, J Biol Inorg Chem*. 2006;11:398–408.
- <sup>13</sup>Gillner DM, Bienvenue DL, Nocek BP, Joachimiak A, Zachary V, Bennett B, Holz RC. The *dapE*-Encoded *N*-Succinyl-L,L-Diaminopimelic Acid Desuccinylase from *Haemophilus influenzae* Contains two Active Site Histidine Residues. *JBIC, J Biol Inorg Chem*. 2009;14:1–10.
- <sup>14</sup>Gillner D, Armoush N, Holz RC, Becker DP. Inhibitors of bacterial *N*-succinyl-L,L-diaminopimelic acid desuccinylase (DapE) and demonstration of in vitro antimicrobial activity. *Bioorg Med Chem Lett*. 2009;19:6350–6352.
- <sup>15</sup>Gillner D, Becker D, Holz R. Lysine biosynthesis in bacteria: a metallodesuccinylase as a potential antimicrobial target. *JBIC, J Biol Inorg Chem*. 2013;18:155–163.
- <sup>16</sup>Nocek BP, Gillner DM, Fan Y, Holz RC, Joachimiak A. Structural Basis for Catalysis by the Mono- and Dimetalated Forms of the *dapE*-Encoded *N*-succinyl-L,L-Diaminopimelic Acid Desuccinylase. *J Mol Biol*. 2010;397:617–626.
- <sup>17</sup>Karita M, Etterbeek ML, Forsyth MH, Tummuru MR, Blaser MJ. Characterization of *Helicobacter pylori* DapE and Construction of a Conditionally Lethal DapE Mutant. *Infect Immun*. 1997;65:4158–4164.
- <sup>18</sup>Jacobsen FE, Lewis JA, Cohen SM. The Design of Inhibitors for Medically Relevant Metalloproteins. *ChemMedChem*. 2007;2:152–171.
- <sup>19</sup>Cosper NJ, Bienvenue DL, Shokes JE, Gilner DM, Tsukamoto T, Scott R, Holz RC. The *dapE*-Encoded *N*-succinyl-L,L-Diaminopimelic Acid Desuccinylase from *Haemophilus influenzae* is a Dinuclear Metallohydrolase. *J Am Chem Soc*. 2003;125:14654–14655.
- <sup>20</sup>Lin Y, Myhrman R, Schrag ML, Gelb MH. Bacterial *N*-succinyl-L-Diaminopimelic Acid Desuccinylase. Purification, Partial Characterization, and Substrate Specificity. *J Biol Chem*. 1988;263:1622–1627.
- <sup>21</sup>Nocek B, Starus A, Makowska-Grzyska M, Gutierrez B, Sanchez S, Jedrzejczak R, Mack JC, Olsen KW, Joachimiak A, Holz RC. The Dimerization Domain in DapE Enzymes Is required for Catalysis. *PLoS One*. 2014;9:e93593.
- <sup>22</sup>Aslanidis C, de Jong PJ. Ligation-independent cloning of PCR products (LIC-PCR) *Nucleic Acids Res*. 1990;18:6069–6074.
- <sup>23</sup>Kim Y, Babnigg G, Jedrzejczak R, Eschenfeldt WH, Li H, Maltseva N, Hatzos-Skintges C, Gu M, Makowska-Grzyska M, Wu R, An H, Chhor G, Joachimiak A. High-throughput protein purification and quality assessment for crystallization. *Methods*. 2011;55:12–28.

- <sup>24</sup>Bienvenue DL, Gilner DM, Davis RS, Bennett B, Holz RC. Substrate Specificity, Metal Binding Properties, and Spectroscopic Characterization of the *dapE*-Encoded-*N*-succinyl-L,L-Diaminopimelic Acid Desuccinylase from *Haemophilus influenzae*. *Biochemistry*. 2003;42:10756–10763.
- <sup>25</sup>Bergmann M, Stein WH. Naphthalene- $\beta$ -sulfonic acid as a reagent for amino acids. *J Biol Chem*. 1939;129:609–618.
- <sup>26</sup>D'souza VM, Holz RC. The Methionyl Aminopeptidase from *Escherichia coli* is an Iron(II) Containing Enzyme. *Biochemistry*. 1999;38:11079–11085.
- <sup>27</sup>Riley MJ. *VTVH 2.1.1 Program for the Simulation and Fitting Variable Temperature-Variable Field MCD Spectra*. The University of Queensland; Brisbane, Australia: 2008.
- <sup>28</sup>Ely F, Hadler K, Mitić N, Gahan L, Ollis D, Plugis N, Russo M, Larrabee J, Schenk G. Electronic and geometric structures of the organophosphate-degrading enzyme from *Agrobacterium radiobacter* (OpdA) *JBIC, J Biol Inorg Chem*. 2011;16:777–787.
- <sup>29</sup>Paulat FLN, Lehnert N. Detailed Assignment of the Magnetic Circular Dichroism and UVvis Spectra of Five-Coordinate High-Spin Ferric [Fe(TPP)(Cl)] *Inorg Chem*. 2008;47:4963–4976.
- <sup>30</sup>Nocek B, Mulligan R, Bargassa M, Collart F, Joachimiak A. Crystal structure of aminopeptidase N from human pathogen *Neisseria meningitidis*. *Proteins: Struct, Funct, Genet*. 2008;70:273–279.
- <sup>31</sup>Rosenbaum G, Alkire RW, Evans G, Rotella FJ, Lazarski K, Zhang RG, Ginell SL, Duke N, Naday I, Lazarz J, Molitsky MJ, Keefe L, Gonczy J, Rock L, Sanishvili R, Walsh MA, Westbrook E, Joachimiak A. The Structural Biology Center 19ID undulator beamline: facility specifications and protein crystallographic results. *J Synchrotron Radiat*. 2006;13:30–45.
- <sup>32</sup>Minor W, Cymborowski M, Otwinowski Z, Chruszcz M. HKL-3000: the integration of data reduction and structure solution - from diffraction images to an initial model in minutes. *Acta Crystallogr, Sect D: Biol Crystallogr*. 2006;62:859–866.
- <sup>33</sup>Emsley PCK. Coot: model-building tools for molecular graphics. *Acta Crystallogr, Sect D: Biol Crystallogr*. 2004;60:2126–2132.
- <sup>34</sup>Murshudov GN, Vagin AA, Dodson EJ. Refinement of Macromolecular Structures by the Maximum-Likelihood Method. *Acta Crystallogr, Sect D: Biol Crystallogr*. 1997;53:240–255.
- <sup>35</sup>Adams PD, Afonine PV, Bunkoczi G, Chen VB, Davis IW, Echols N, Headd JJ, Hung LW, Kapral GJ, Grosse-Kunstleve RW, McCoy AJ, Moriarty NW, Oeffner R, Read RJ, Richardson DC, Richardson JS, Terwilliger TC, Zwart PH. PHENIX: a comprehensive Python-based system for macromolecular structure solution. *Acta Crystallogr, Sect D: Biol Crystallogr*. 2010;66:213–221.

- <sup>36</sup>Laskowski RA, MacArthur MW, Moss DS, Thornton JM. PROCHECK: a program to check the stereochemical quality of protein structures. *J Appl Crystallogr.* 1993;26:283–291.
- <sup>37</sup>Davis IW, Leaver-fay A, Chen VB, Block JN, Kapral GJ, Wang X, Murray LW, Arendall WB, Snoeyink J, Richardson JS, Richardson DC. MolProbity: all-atom contacts and structure validation for proteins and nucleic acids. *Nucleic Acids Res.* 2007;35:W375–W383.
- <sup>38</sup>Eufri DSA, Sironi A. Smile - Shaded Molecular imaging on low-cost equipment. *J Mol Graphics.* 1989;7:184.
- <sup>39</sup>Bennett B. EPR of Cobalt-Substituted Zinc Enzymes. In Metals in Biology: Applications of High Resolution EPR to Metalloenzymes. In: Hanson G, Berliner L, editors. *Biological Magnetic Resonance, Metals in Biology.* Springer; New York: 2010. pp. 345–370.
- <sup>40</sup>Larrabee JA, Schenk G, Mitic N, Riley MJ. Use of magnetic circular dichroism to study dinuclear metallohydrolases and the corresponding biomimetics. *Eur Biophys J.* 2015 doi: 10.1007/s00249-015-1053-6.
- <sup>41</sup>Kaden TA, Holmquist B, Vallee BL. Magnetic circular dichroism of cobalt(II) complexes. *Inorg Chem.* 1974;13:2585–2590.
- <sup>42</sup>Larrabee JA, Alessi CM, Asiedu ET, Cook JO, Hoerning KR, Klingler LJ, Okin GS, Santee SG, Volkert TL. Magnetic circular dichroism spectroscopy as a probe of geometric and electronic structure of cobalt(II)-substituted proteins: Ground-state zero-field splitting as a coordination number indicator. *J Am Chem Soc.* 1997;119:4182–4196.
- <sup>43</sup>Harding MJ, Briat B. The electronic absorption and magnetic circular dichroism spectra of cobalt (II) bromate hexahydrate. *Mol Phys.* 1973;25:745–776.
- <sup>44</sup>Daumann LJ, Comba P, Larrabee JA, Schenk G, Stranger R, Cavigliasso G, Gahan LR. Synthesis, Magnetic Properties, and Phosphoesterase Activity of Dinuclear Cobalt(II) Complexes. *Inorg Chem.* 2013;52:2029–2043.
- <sup>45</sup>Larrabee JA, Chyun SA, Volwiler AS. Magnetic Circular Dichroism Study of a Dicobalt(II) Methionine Aminopeptidase/Fumagillin Complex and Dicobalt II–II and II–III Model Complexes† *Inorg Chem.* 2008;47:10499–10508.
- <sup>46</sup>Larrabee JA, Johnson WR, Volwiler AS. Magnetic Circular Dichroism Study of a Dicobalt(II) Complex with Mixed 5- and 6-Coordination: A Spectroscopic Model for Dicobalt(II) Hydrolases. *Inorg Chem.* 2009;48:8822–8829.
- <sup>47</sup>Badger J, Sauder JM, Adams JM, Antonysamy S, Bain K, Bergseid MG, Buchanan SG, Buchanan MD, Batiyenko Y, Christopher JA, Emtage S, Eroshkina A, Feil I, Furlong EB, Gajiwala KS, Gao X, He D, Hendle J, Huber A, Hoda K, Kearins P, Kissinger C, Laubert B, Lewis HA, Lin J, Loomis K, Lorimer D, Louie G, Maletic M, Marsh CD, Miller I, Molinari J,

- Muller-Dieckmann HJ, Newman JM, Noland BW, Pagarigan B, Park F, Peat TS, Post KW, Radojicic S, Ramos A, Romero R, Rutter ME, Sanderson WE, Schwinn KD, Tresser J, Winhoven J, Wright TA, Wu L, Xu J, Harris TJR. Structural analysis of a set of proteins resulting from a bacterial genomics project. *Proteins: Struct, Funct, Genet*. 2005;60:787–796.
- <sup>48</sup>Makinen MW, Yim MB. Coordination environment of the active-site metal ion of liver alcohol dehydrogenase. *Proc Natl Acad Sci U S A*. 1981;78:6221–6225.
- <sup>49</sup>Turpeinen U, Ahlgren M, Haämaälääinen R. Structures of di- $\mu$ -acetato-(O,O')- $\mu$ -aqua-bis[acetato(N,N,N',N'-tetramethylethylenediamine)cobalt(II) and  $\mu$ -aqua-di- $\mu$ -chloroacetato-(O,O')-bis[chloroacetato(N,N,N',N'-tetramethylethylenediamine)-cobalt(II) *Acta Crystallogr, Sect B: Struct Crystallogr Cryst Chem*. 1982;38:1580–1583.
- <sup>50</sup>Chaudhuri P, Ouerbach J, Wieghardt K, Nuber B, Weiss J. Synthesis, electrochemistry, and magnetic properties of binuclear cobalt complexes containing the  $\text{Co}_2(\mu\text{-X})(\mu\text{-carboxylato})_2^{+n}$  core (X=OH, Cl, or Br; n=1–3) *J Chem Soc, Dalton Trans*. 1990:271–278.
- <sup>51</sup>Ustynyuk L, Bennett B, Edwards T, Holz RC. Inhibition of the Aminopeptidase from *Aeromonas proteolytica* by Aliphatic Alcohols. Characterization of the Hydrophobic Substrate Recognition Site. *Biochemistry*. 1999;38:11433–11439.
- <sup>52</sup>Chen G, Edwards T, D'souza VM, Holz RC. Mechanistic studies on the aminopeptidase from *Aeromonas proteolytica*: A two-metal ion mechanism for peptide hydrolysis. *Biochemistry*. 1997;36:4278–4286.
- <sup>53</sup>Lowther WT, Matthews BW. Metalloaminopeptidases: Common Functional Themes in Disparate Structural Surroundings. *Chem Rev*. 2002;102:4581–4607.

**\*Corresponding Authors:** Department of Chemistry, Marquette University, 535 N. 14th St., Milwaukee, WI 53201-1881. [richard.holz@marquette.edu](mailto:richard.holz@marquette.edu). Phone: (414) 288-7230. Fax: (414) 288-7066; Center for Structural Genomics of Infectious Diseases, Computation Institute, University of Chicago, 5735 S. Ellis Ave., Chicago, IL 60637. [andrzej@uci.edu](mailto:andrzej@uci.edu). Phone: (630) 252-3926. Fax: (630) 252-6991

## Supplementary Material

**Supporting Information for**

**Inhibition of the *dapE*-encoded *N*-succinyl-L,L-diaminopimelic acid  
desuccinylase from *Neisseria meningitidis* by L-Captopril.**

Anna Starus<sup>1</sup>, Boguslaw Nocek<sup>2</sup>, Brian Bennett<sup>3</sup>, James A. Larrabee<sup>4</sup>, Daniel L. Shaw<sup>4</sup>, Wisath  
Sae-Lee<sup>4</sup>, Marie T. Russo<sup>4</sup>, Danuta M. Gillner<sup>5</sup>, Magdalena Makowska-Grzyska<sup>2</sup>, Andrzej  
Joachim<sup>2\*</sup>, and Richard C. Holz<sup>6\*</sup>

<sup>1</sup>*The Department of Chemistry and Biochemistry, Loyola University-Chicago, 1068 W. Sheridan  
Rd., Chicago, IL 60626,* <sup>2</sup>*Center for Structural Genomics of Infectious Diseases, Computation  
Institute, University of Chicago, 5735 South Ellis Avenue, Chicago, IL 60637,* <sup>3</sup>*Department of  
Physics, Marquette University, Milwaukee, Wisconsin 53201,* <sup>4</sup>*Department of Chemistry and  
Biochemistry, Middlebury College, Middlebury, Vermont 05753,* <sup>5</sup>*Department of Chemistry,  
Silesian University of Technology, 44-100 Gliwice, Poland,* <sup>6</sup>*Department of Chemistry,  
Marquette University, Milwaukee, Wisconsin 53201*



**Figure SI-1.** MCD spectra of *NmDapE* with 1 and 2 eq. of added  $\text{Co}^{2+}$ . The enzyme concentration was 29 mg/mL in 60/40 (v/v) glycerol/buffer (0.70 mM in protein, 1.4 mM in active sites). The spectra were recorded at 1.5 K and 7.0 T in a 0.63 cm path length cell. The MCD peaks due to four-coordinate (4-C) and six-coordinate (6-C)  $\text{Co}^{2+}$  are indicated. The binding affinities of both sites appear to be nearly equal.

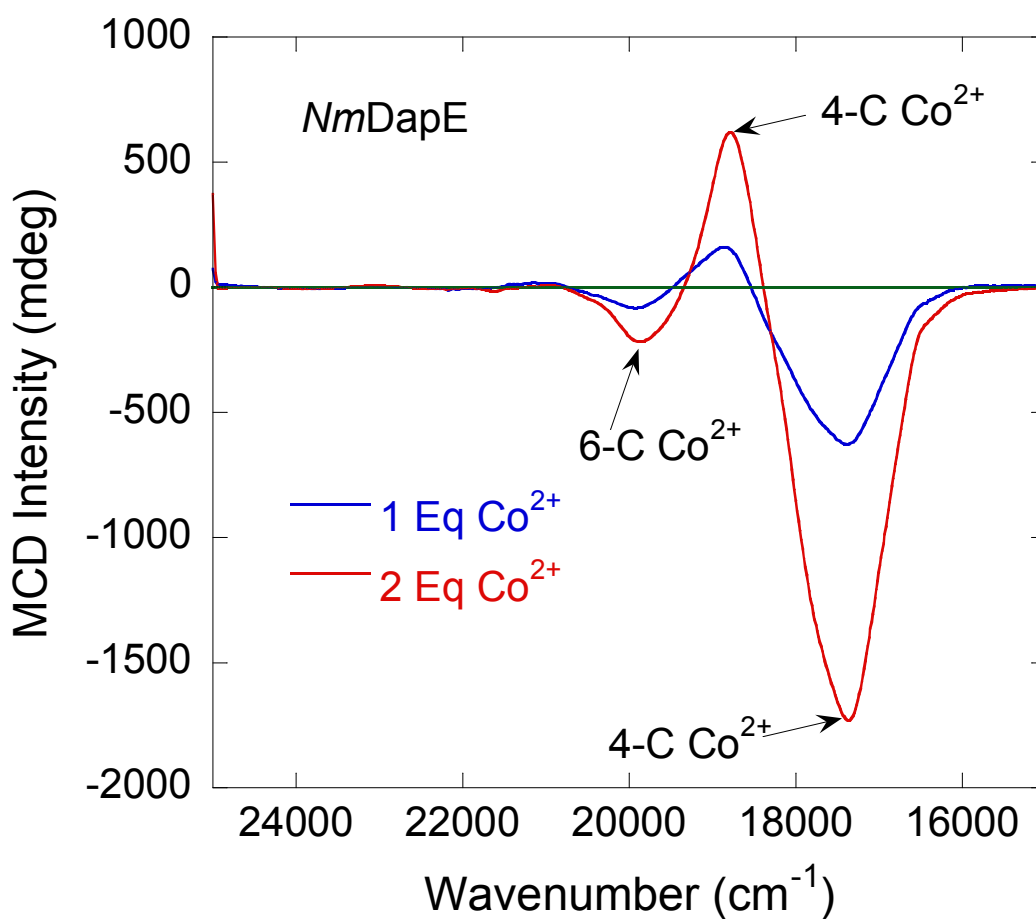


**Figure SI-2.** MCD spectra of *HiDapE* with 1 and 2 eq. of added  $\text{Co}^{2+}$ . The enzyme concentration was 33 mg/mL in 60/40 (v/v) glycerol/buffer (0.80 mM in protein, 1.6 mM in active sites). The spectra were recorded at 1.5 K and 7.0 T in a 0.63 cm path length cell. The MCD peaks due to four-coordinate (4-C) and six-coordinate (6-C)  $\text{Co}^{2+}$  are indicated. The binding affinity of the four-coordinate site appears to be much higher than the six-coordinate site.

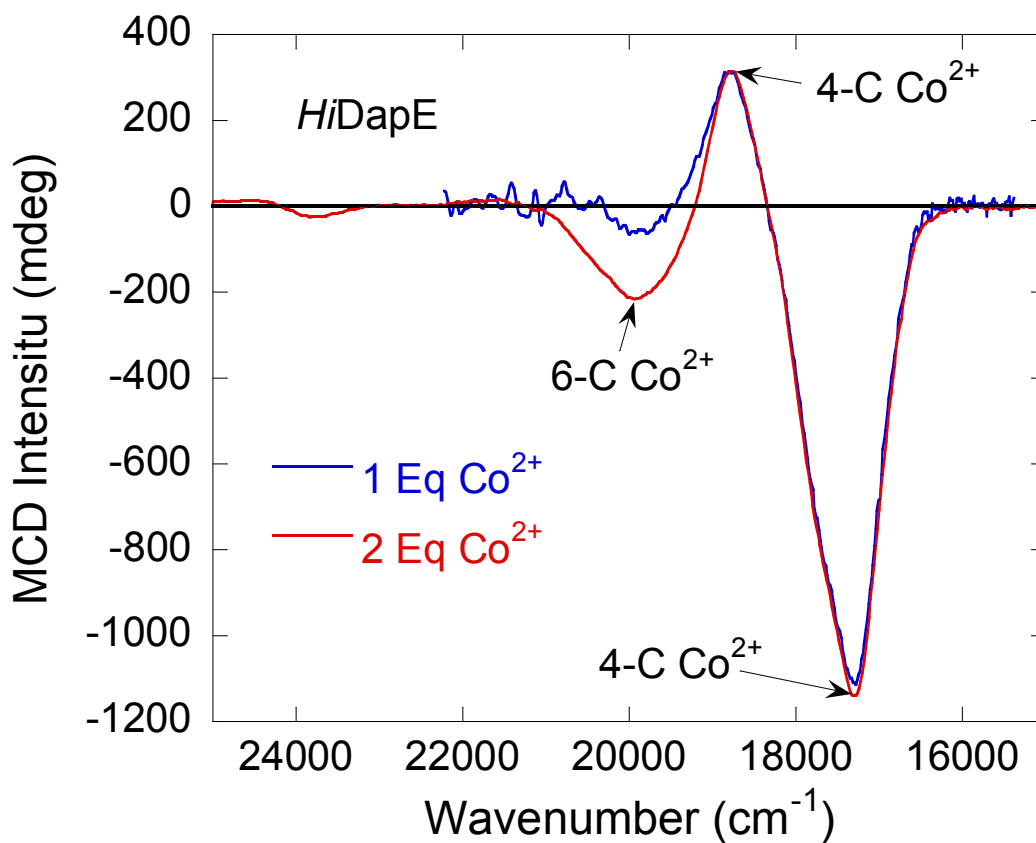


**Figure SI-3.** Magnetization plot of the VTVH MCD data collected on the 503 nm band in CoCoNmDapE. Key ground state electronic parameters are given in the figure and are typical for six-coordinate high-spin  $\text{Co}^{2+}$ .

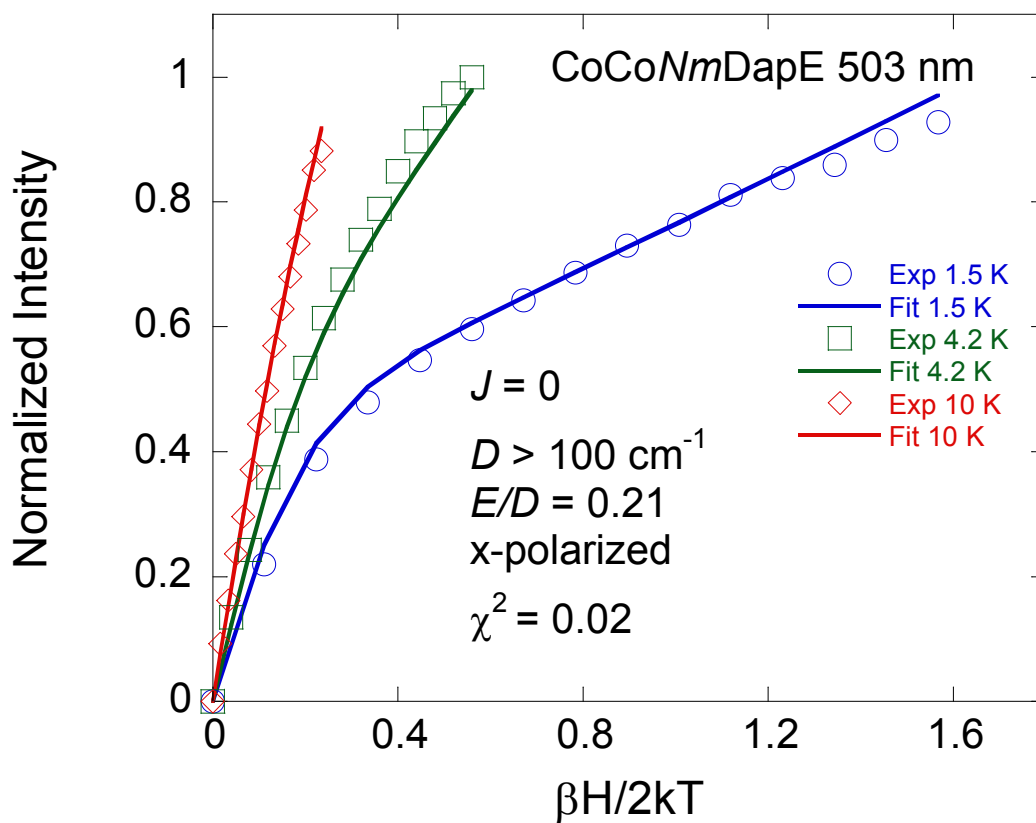


**Figure SI-4.** Magnetization plot of the VTVH MCD data collected on the 503 nm band in CoCoHiDapE. Key ground state electronic parameters are given in the figure and are typical for six-coordinate high-spin  $\text{Co}^{2+}$ .

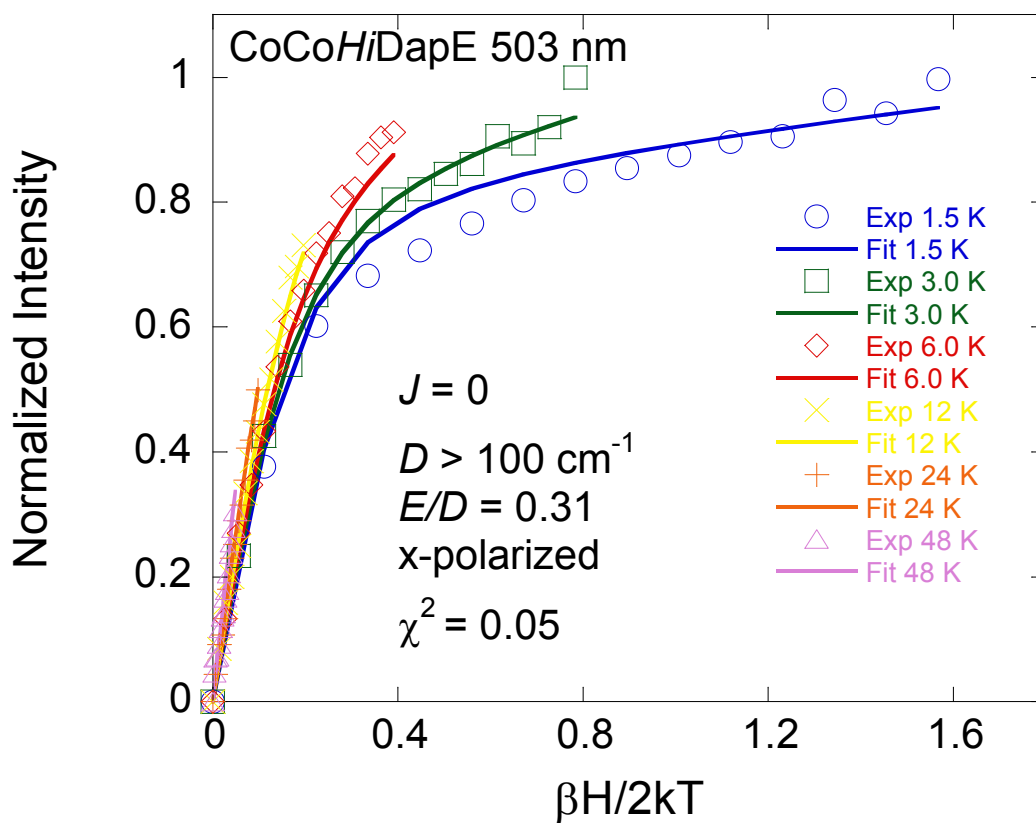


**Figure SI-5.** Magnetization plot of the VTVH MCD data collected on the 532 nm band in CoCoNmDapE. Key ground state electronic parameters are given in the figure and are typical for four-coordinate high-spin  $\text{Co}^{2+}$ .

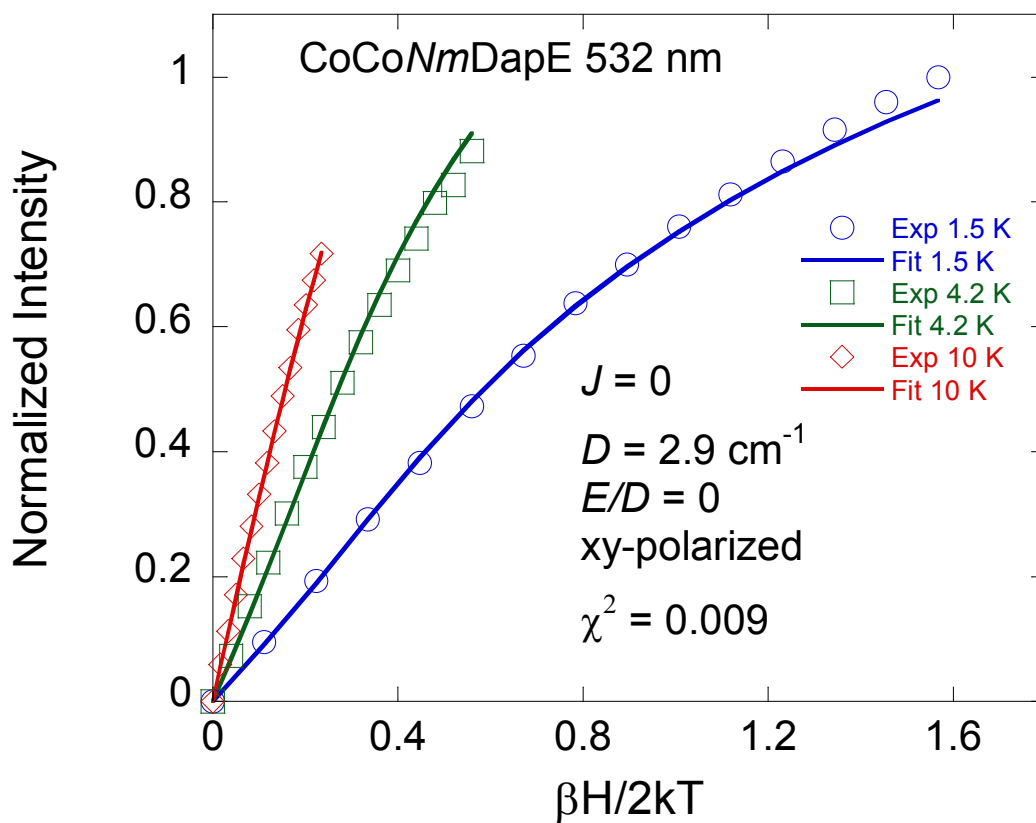


**Figure SI-6.** Magnetization plot of the VTVH MCD data collected on the 532 nm band in CoCoHiDapE. Key ground state electronic parameters are given in the figure and are typical for four-coordinate high-spin  $\text{Co}^{2+}$ .

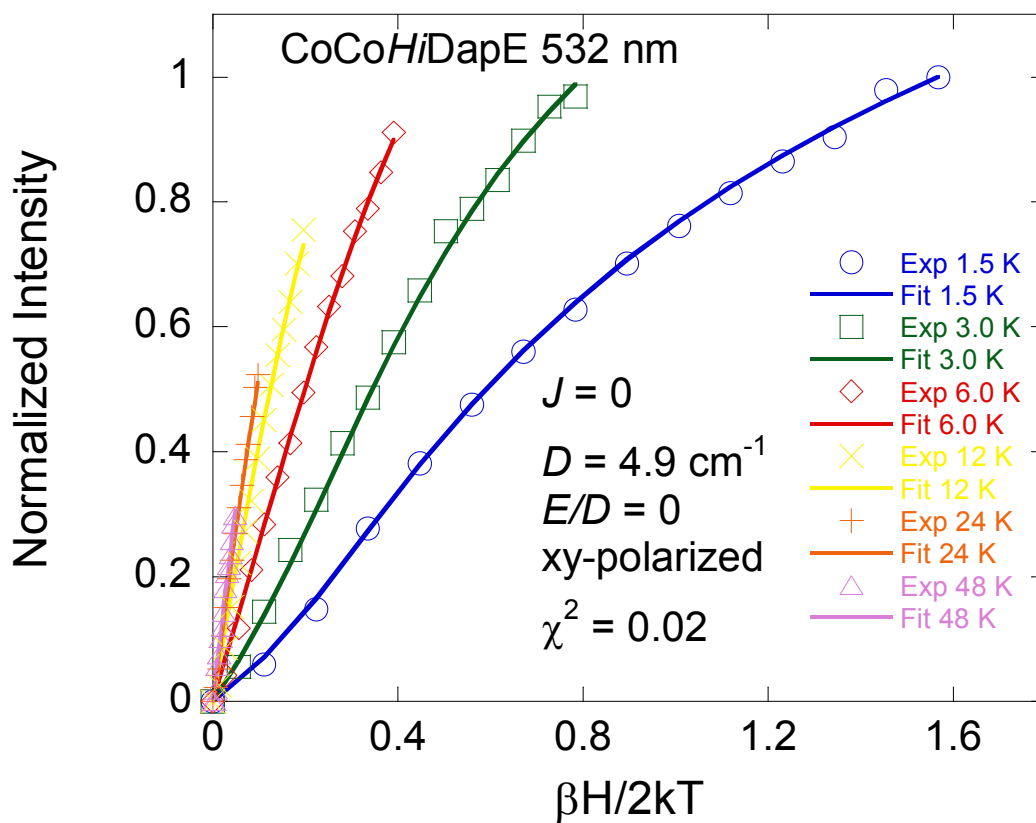




**Figure SI-7.** Magnetization plot of the VTVH MCD data collected on the 576 nm band in CoCoNmDapE. Key ground state electronic parameters are given in the figure and are typical for four-coordinate high-spin  $\text{Co}^{2+}$ .

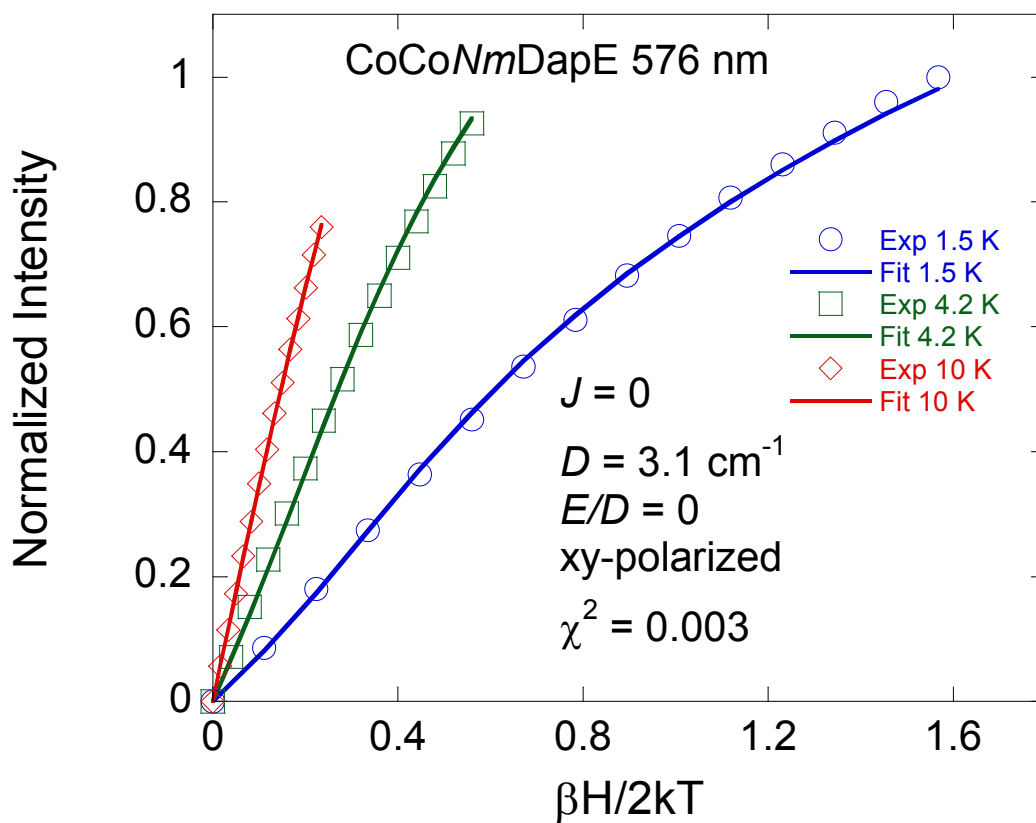


**Figure SI-8.** Magnetization plot of the VTVH MCD data collected on the 576 nm band in CoCoHiDapE. Key ground state electronic parameters are given in the figure and are typical for four-coordinate high-spin  $\text{Co}^{2+}$ .

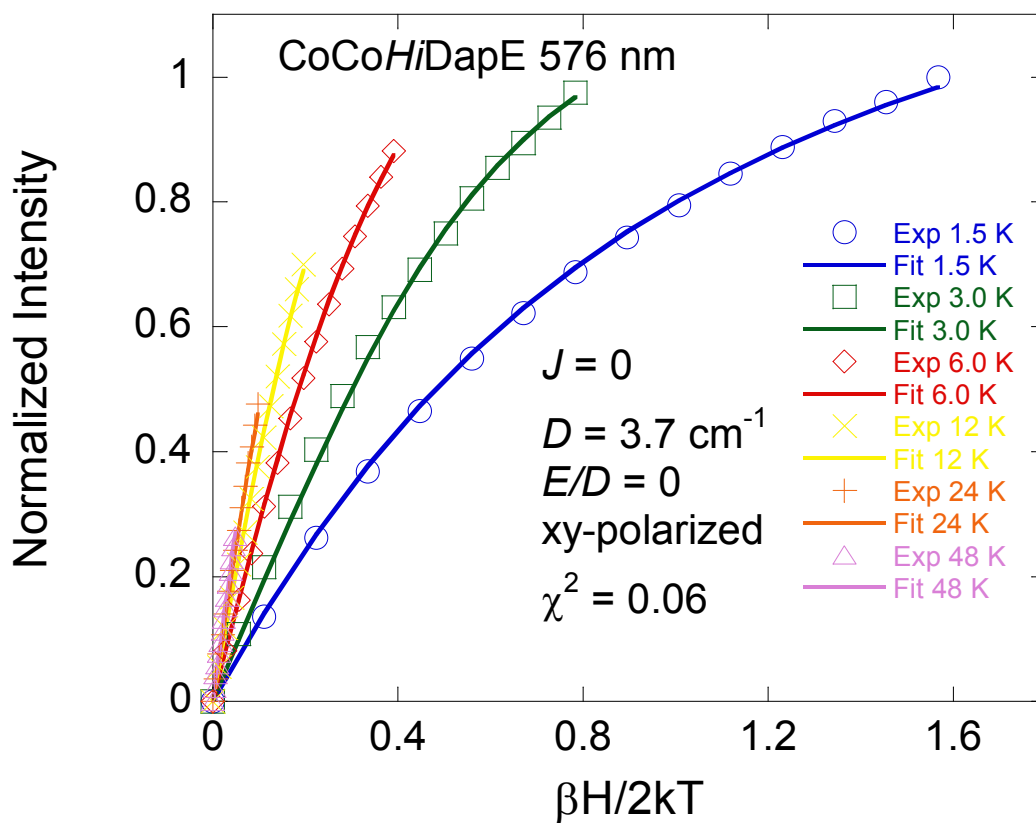


**Figure SI-9.** Magnetization plot of the VTVH MCD data collected on the 505 nm band in CoCo*HiDapE* with 5 eq. of captopril. Key ground state electronic parameters are given in the figure and are typical for four-coordinate high-spin  $\text{Co}^{2+}$ .

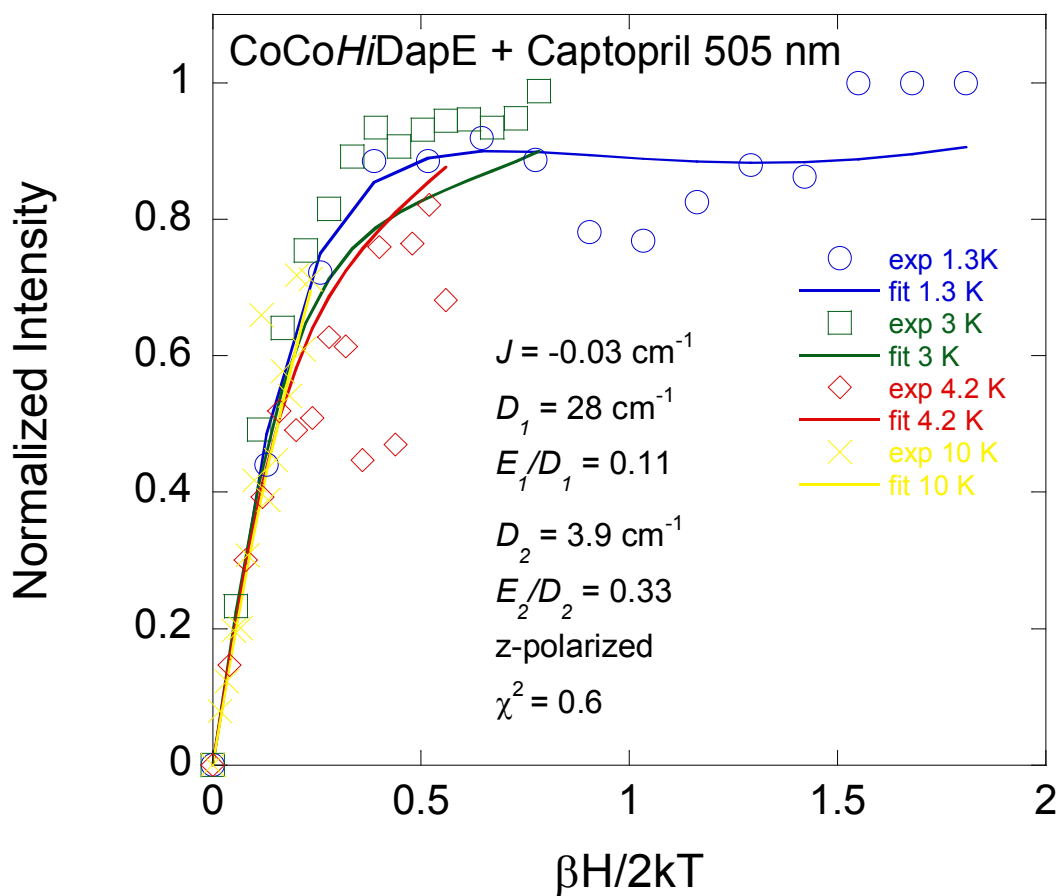


**Figure SI-10.** Magnetization plot of the VTVH MCD data collected on the 530 nm band in CoCoHiDapE with 5 eq. of captopril. Key ground state electronic parameters are given in the figure and are typical for four-coordinate high-spin  $\text{Co}^{2+}$ .

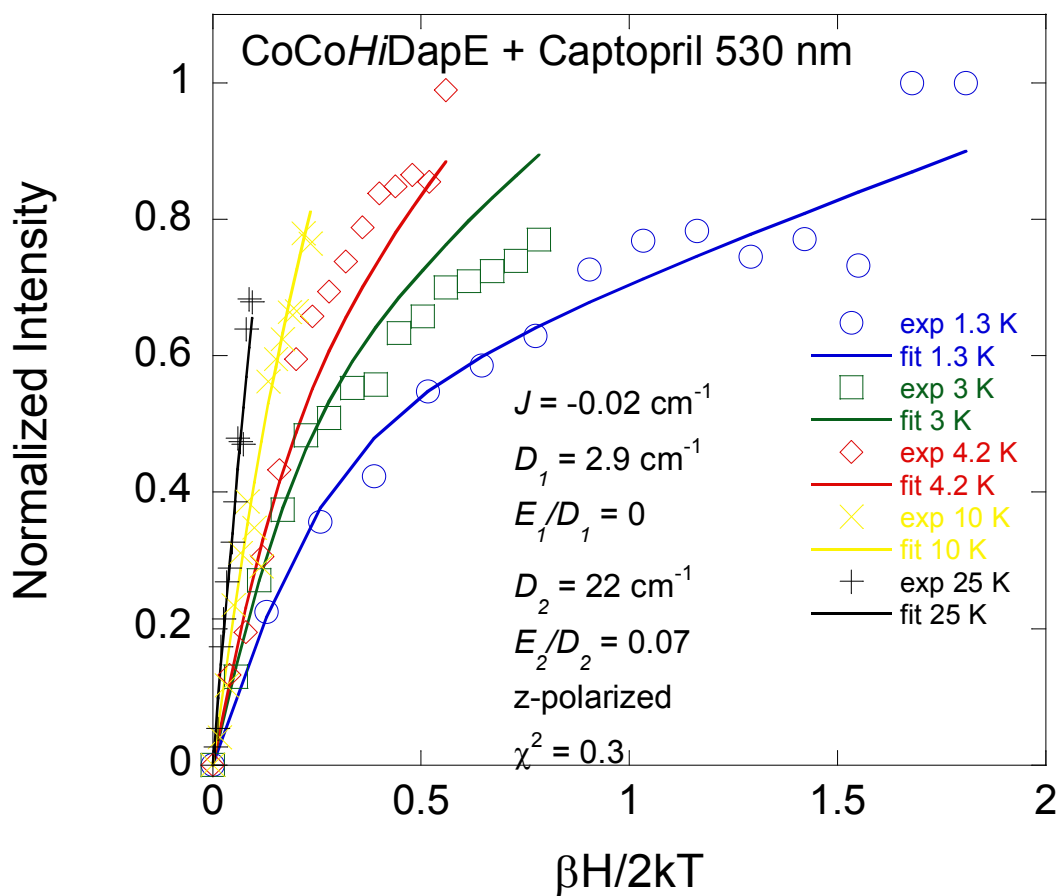


**Figure SI-11.** Magnetization plot of the VTVH MCD data collected on the 604 nm band in CoCoNmDapE with 5 eq. of captopril. Key ground state electronic parameters are given in the figure and are typical for four-coordinate high-spin  $\text{Co}^{2+}$ .

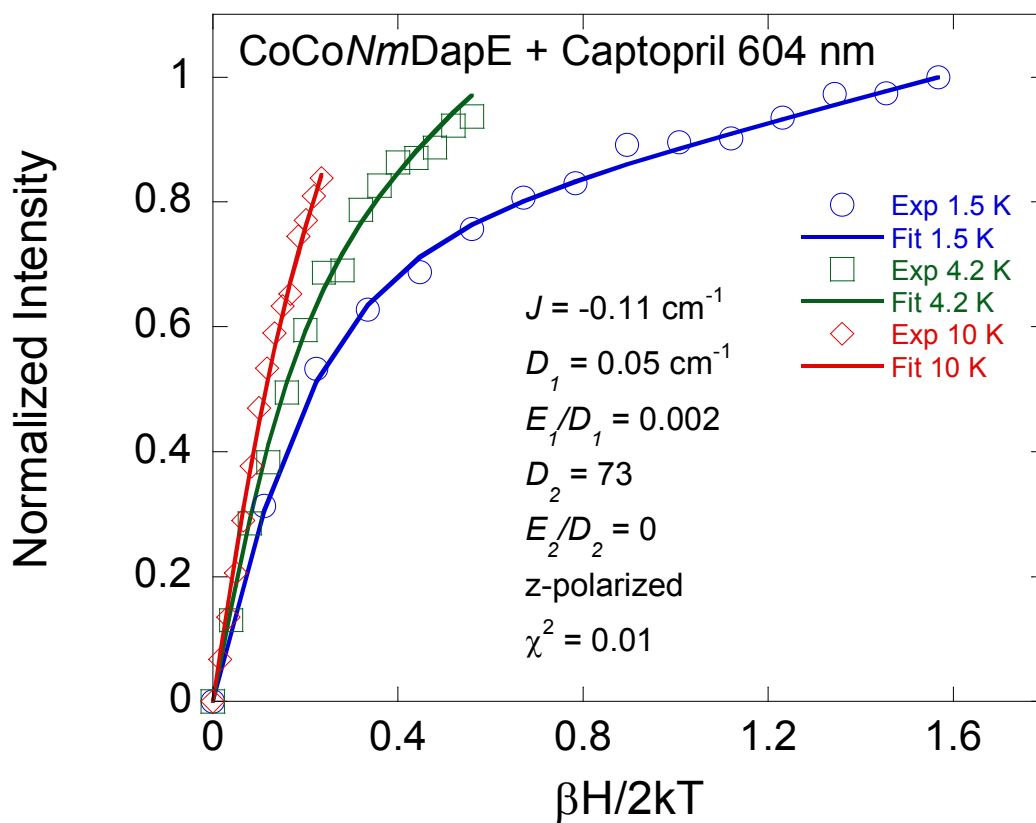


**Figure SI-12.** Magnetization plot of the VTVH MCD data collected on the 604 nm band in CoCoHiDapE with 5 eq. of captopril. Key ground state electronic parameters are given in the figure and are typical for four-coordinate high-spin  $\text{Co}^{2+}$ .

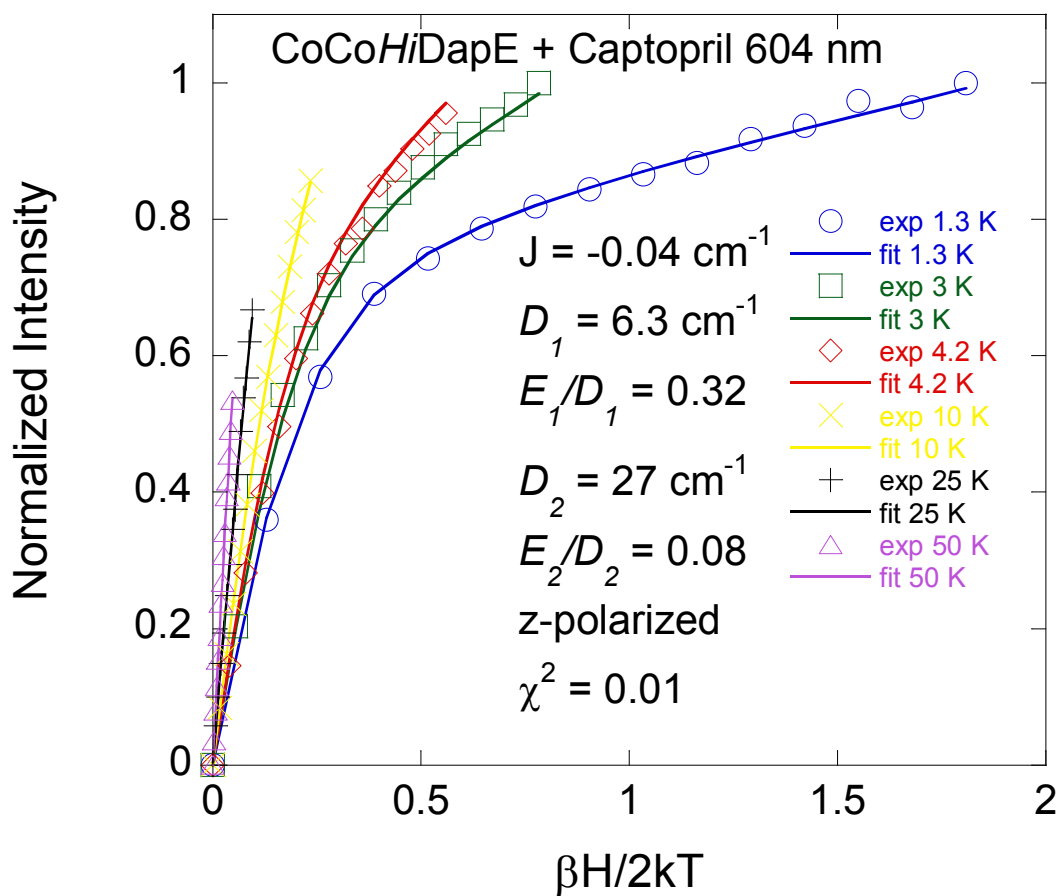




**Figure SI-13.** (A) Structure of  $[\text{Co}_2(\mu\text{-OH})(\mu\text{-1,3-CF}_3\text{COO})_2(\text{Me}_3\text{TACN})_2]^+$ . (B) MCD spectrum of  $[\text{Co}_2(\mu\text{-OH})(\mu\text{-1,3-CF}_3\text{COO})_2(\text{Me}_3\text{TACN})_2]^+$  in ethanol taken at 1.3 K and 7.0 T. (C) Magnetization plot for the 462 nm band of the complex. The complex was synthesized according to Lachicotte, R.; Kitayforodskiy, A.; Hagen, K. S. *J. Am. Chem. Soc.* **1993**, *115*, 8883-8884.

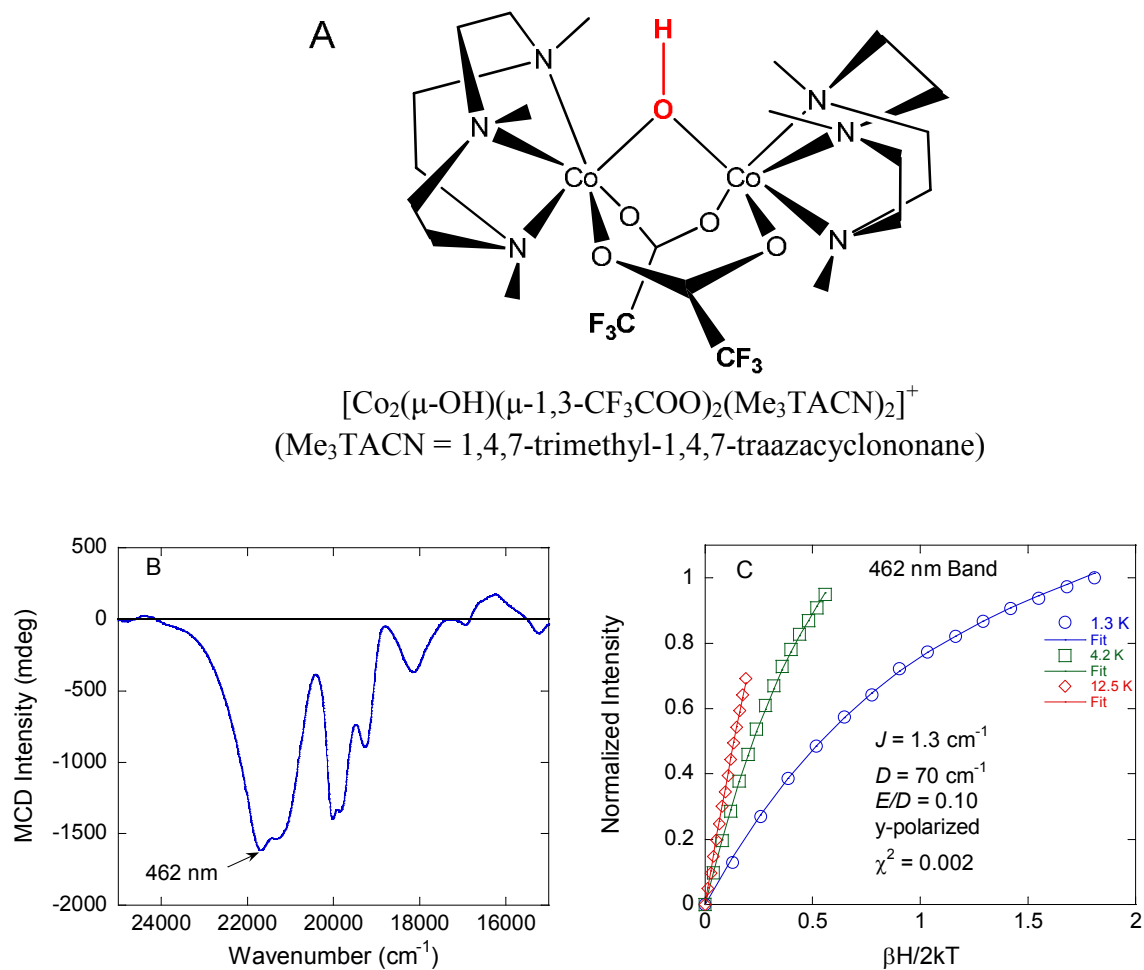


**Figure SI-14.** (A) Structure of **CoF** and **CoH**. (B) MCD spectra of **CoH** and **CoF**. The spectrum of **CoH** was taken as a solid mull at 1.3 K and 7.0 T. The spectrum of **CoF** was taken as a 2.5 mM solution in EtOH at 1.3 K and 7.0 T. (C) Magnetization plot for the 497 nm band of **CoF**. The VTVH MCD data from CoH were also fitted (not shown) and the fit parameters are:  $J = -0.65 \text{ cm}^{-1}$ ,  $D = 64 \text{ cm}^{-1}$ ,  $E/D = 0.33$ , y-polarized,  $\chi^2 = 0.07$ . **CoF** and **CoH** were synthesized according to Lachicotte, R.; Kitayforodskiy, A.; Hagen, K. S. *J. Am. Chem. Soc.* **1993**, *115*, 8883-8884.

